Hindawi
Advances in Civil Engineering
Volume 2023, Article ID 5398662, 24 pages
https://doi.org/10.1155/2023/5398662

Research Article

Experimental Study and Numerical Simulation Analysis on Reinforcement of Mortise-Tenon Joints with Flat Steel Strips

Shurong Gan,[1,2] **Wen Pan**,[1,2] **Hexian Su**,[1,2] **Yucheng Jin**,[1,2] **Chuanwei Zhu**,[1,2] **and Shibin Yu**[1,2]

[1]*Faculty of Civil Engineering and Mechanics, Kunming University of Science and Technology, Kunming 650500, China*
[2]*Earthquake Engineering Researching Center of Yunnan, Kunming University of Science and Technology, Kunming 650500, China*

Correspondence should be addressed to Hexian Su; sxhh870@qq.com

Received 14 October 2022; Revised 31 January 2023; Accepted 6 February 2023; Published 2 March 2023

Academic Editor: Angelo Aloisio

To study the aseismic performance after the reinforcement of the mortise-tenon joints of folk houses with traditional Chuan-Dou style wood structure and their steel plate, test specimens of joints—two for Tou mortise-tenon joints, two for Ban mortise-tenon joints, and two for dovetail mortise-tenon joints—were fabricated out of hemlock, and steel plates were utilized to reinforce one of the joint specimens of each type on the middle part of the mortise-tenon joint. By carrying out pseudo-static tests on the joints and building ABAQUS numerical model; the position where the mortise-tenon joints were to be reinforced by the steel plates was optimized for a comparative analysis into the test results on reinforced and unreinforced mortise-tenon joints and the numerically simulated bending moment-turning angle hysteresis curve, skeleton curve, energy-dissipating capacity, and rigidity degeneration curves. The results showed the following: the pulling-out phenomenon of tenons was severe, and the aseismic performance of Tou tenons was superior to Ban tenons and dovetail tenons; reinforcing the middle part of mortise-tenon joints with steel plates could effectively reduce the pulling-out amount of joints and promote the aseismic performance of mortise-tenon joints but have an insignificant promotive effect for the bearing capacity of Tou mortise-tenon joints; the aseismic performance was improved significantly after the flat steel strip reinforced position was moved to the upper and lower ends of mortise-tenon joints, with the ultimate bearing capacities being 1.5~2.4 times that on the middle part of flat steel strip reinforced joints.

1. Introduction

Due to its aesthetic appearance, solidity, livability, and other features, the wooden structure is popular worldwide, particularly in China, Canada, Japan, and the US [1–3]. Traditional Chinese wood structure folk houses enjoy a long history, evolving into distinct architectural styles for different climatic, geographical, and cultural factors. The wooden structures in Southwest China are predominated by the Chuan-Dou style timber frame [4–6]. The mortise-tenon joint types of Chuan-Dou style timber frames mainly include straight tenon, Tou tenon, Ban tenon, and dovetail tenon [7–13], as shown in Figure 1. In economically underdeveloped areas, there remain a vast majority of unprotected wooden structure architectures playing the vital roles as dwellings, ancestral halls, and so on. Despite the excellent deformability and bearing capacity of traditional wooden structure folk houses, most such architectures are prone to pulling-out, shedding, and other phenomena of instability or even breakdown of joints after undergoing an earthquake [13]. The traditional wooden structure has suffered from various destructions while used for a long period, so that its current status turns out unoptimistic [14, 15]. Therefore, a growing attention has been paid to the studies on the protection and reinforcement of traditional wooden structure folk houses.

Over the recent years, numerous scholars have started to pay attention to reinforcement experiment research and finite element analysis (FEA) on wooden structure folk houses. By examining the Chinese wooden structure

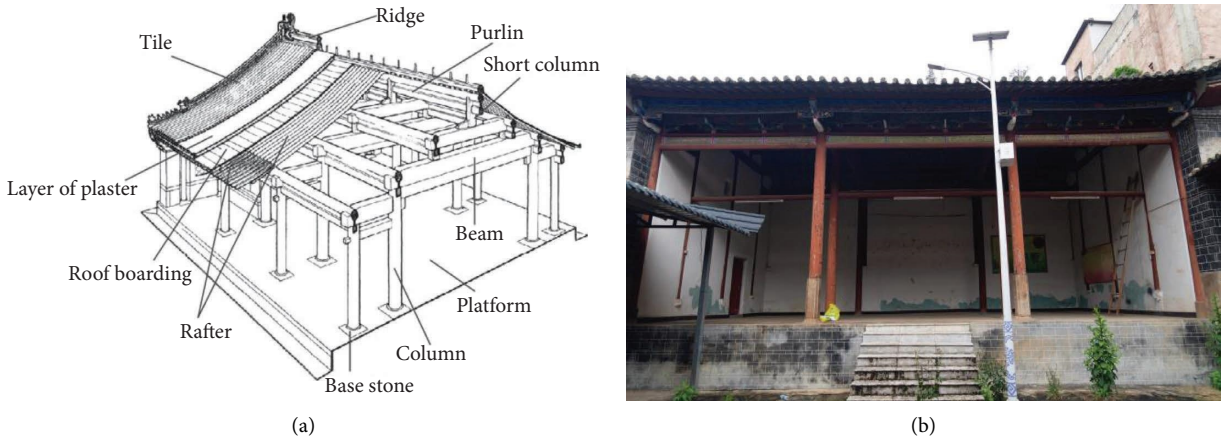

Figure 1: Traditional Chuan-Dou style wooden structure: (a) 3D view of timber frame with laminated beams and columns. (b) A typical Chuan-Dou style wooden structure folk house in Southwest China.

architectures of Song Dynasty, Li et al. [16] conducted a low-cycle repeated loading test and analyzed the energy-dissipating capacity of wooden structure frames with 1 : 4 dovetail mortise-tenon joints. Chun et al. [17] conducted low-cycle repeated loading tests on four typical types of mortise-tenon joint specimens with traditional Chinese southern wooden structures, analyzing and comparing the damage modes, hysteresis curves, skeleton curves, and rotational rigidities of these different mortise-tenon joints. Through low-cycle repeated loading test and shaking table test on a traditional timber frame, Zhang et al. [18] studied the connective property and energy-dissipating capacity of mortise-tenon joints and the aseismic performance of the overall structure. By carrying out a low-cycle repeated loading test on Tou mortise-tenon joints, Xue et al. [19] sequentially analyzed the aseismic performance of the joints, adopted ABAQUS for numerical simulation of the test, and studied the connective property and energy-dissipating capacity of Tou mortise-tenon joints and the effect of depth of a section on aseismic performance. Shi et al. [20] adopted finite element software to simulate the stress condition of dowelled Tou mortise-tenon joints under the monotonic loading test and conducted a comparative analysis with the theoretical model and test data, which indicated a good coincidence among the three. With the hall of Baoguo Temple in Ningbo, China, as the prototype, Lin et al. [21] built a simplified numerical model and proposed a performance evaluation method applicable to traditional wooden structures. Chen and Qiu [22, 23] employed ABAQUS simulation and testing to build a bending moment-turning angle mechanical model for Tou and straight mortise-tenon joints and conducted a comparative analysis, and simplified the bending moment-turning angle relations when the joints were loaded into a three broken line model. In order to study the antishear performance of tenons, Okamoto et al. [24] performed a shearing test on specimens with crevices in the upper and lower parts of tenons and thereon proposed a formula for the bending strength of creviced beam ends. Xie et al. [25] built finite element models under different pulling-out degrees of tenons and studied the effect of pulling-out amount on the hysteretic behaviors of joints. The results showed the following: the more significantly the joint was pulled out, the lower its bearing capacity, the weaker its deformability, and the more significant its aseismic performance degradation. In order to study the stress mechanism and mechanical model of a straight tenon with wooden bolt pins, Hu et al. [26] fabricated three sets of full-size models and conducted low-cycle repeated loading tests. In order to study the hysteretic property of ancient architectures, the research group of Chen et al. [27] fabricated a full-size frame model of the wooden structure of Chinese Song Dynasty, conducted pseudo-static tests by exerting three vertical loads on the model, and proposed the limit of the angle of displacement for structure design and the equivalent viscous damping and ductility factor for the dynamic response analysis. Guan et al. [28] built a 3D nonlinear finite element model to simulate the contact stress of mortise-tenon joints under the wedge pressure of different sizes of woken corks and the strain on the column. The results showed that the wooden corks had little impact on the contact stress of the mortise-tenon joints but certain impact on the initial rigidity of the joints. Jin et al. [29] studied the aseismic performances of joints before and after reinforcement by carrying out pseudo-static tests on batten, steel plate, and clincher reinforced mortise-tenon joints. The results showed that all reinforced joints achieved improvement in bearing capacity, with a 5% or so decline in pulling-out amount, and the batten had the most significant reinforcement effect. Based on the contact theory and the contact property of mortise-tenon joints, Xie et al. [30] put forward a normal contact model for mortise-tenon joints, on which basis they built a finite element model for straight tenon joints under the action of low-cycle repeated load. In order to better simulate the model for wooden structure mortise-tenon joints in finite element software, Hu and Liu [31] built three models: the whole rigid model, the tie rigid model, and the semirigid model, to simulate the bearing capacity of mortise-tenon joints and compare with the test data. The results showed that the semirigid model had a high degree of coincidence and that the tenon width had a high

degree of influence on the bearing capacity of mortise-tenon joints. Khelifa and Celzard [32] reinforced a beam for higher bearing capacity via a carbon fiber reinforced polymer (CFRP) and developed and used a subprogram of ABAQUS VUMAT to simulate the elastic-plastic anisotropic bending behavior of timber. Aloisio et al. [33] proposed a simulation method applied to the hysteresis curves of wooden structures and provided the MATLAB and Python codes for development. Meanwhile, they traded off the complexity and accuracy of the hysteresis curves of wooden structures.

In order to further study the methods to reinforce traditional wooden structures with economical efficiency and applicability, this paper conducted a field investigation into a traditional wooden structure folk house in Southwest China; three representative mortise-tenon forms, Tou tenon, Ban tenon, and dovetail tenon, were particularly selected from the southwestern area as prototypes for fabricating the specimens of joints; flat steel strips were utilized to reinforce the mortise-tenon joints on the middle part, and pseudo-static tests were carried out for the systematic analysis into the aseismic performance of the three types of mortise-tenon joints. Meanwhile, the finite element software ABAQUS was adopted to build a numerical model to optimize the position where mortise-tenon joints were to be reinforced by flat steel strips and to further analyze the stress conditions and performances of mortise-tenon joints at different reinforcement positions. This paper is expected to provide a more effective method and basis for the reinforcement of rural wooden structure houses in the future.

2. Experimental Design

2.1. Design and Fabrication of Specimens. With three mortise-tenon types, Tou tenon, Ban tenon, and dovetail tenon, for the typical Chuan-Dou style wooden structure folk house in Southwest China as the prototypes, the common timber hemlock (Latin name: Tsuga chinensis) was selected to be machined and made into specimens by the professional technicians from the Institute for Seismic Research, Kunming University of Science and Technology. The concrete production procedure included the fabrications and assemblies of convex tenons and concave mortises and of reinforcing flat steel strips. Joint types are shown in Figure 2. Mortise-tenon sizes are shown in Table 1. The reinforcement method of joints is shown in Table 2. Sizes of beams and columns are shown in Table 3. The timber for the test was the common hemlock in South China. The standard specimens underwent a material characteristic test by Chinese National Standard GB/T228.1-2010 [34] to obtain their mechanical performance parameters as shown in Tables 4 and 5.

Mortise-tenon joints were reinforced by the flat steel strips made of *Q*235 steel. Each of the two flat steel strips for bilateral reinforcement was 40 mm wide, 425 mm long, and 2 mm thick, and parallel with the beams. The connection method was anchoring with A12 bolts. Reinforcement forms are shown in Figure 3.

2.2. Load Test and Measurement Schemes. This test adopted the displacement control loading system recommended in the specification for the seismic test of buildings (JGJ/T101-2015) [35]. The top and bottom of specimen columns were fixed using steel tube sleeves. A 10 kN vertical constant load was applied on the top of columns using a hydraulic jack, while an electrohydraulic servo actuator was adopted to apply cyclic load 500 mm away from the edge of columns to simulate the vertical load. The loading devices for the test are shown in Figure 4. The beam-end load was exerted on a graded basis via displacement control. Before the test displacement reached the maximum range ±120 mm of the testing device, load was exerted three times with an increment of 10 mm. The test ended upon reaching the maximum range of the testing machine or when the specimens were broken. The loading system is shown in Figure 5.

3. Experimental Results

3.1. Unreinforced Specimens. Under the condition of 10 mm loading amplitude for Tou mortise-tenon joint JD-1a, a creak due to friction and squeezing was made between its convex tenon and concave mortise. Under the same amplitude, the creak in the first loop was louder than those in the second and third loops. Moreover, with the increase in the loading amplitude, the loudness of the sound augmented, so did the compressional deformation, as shown in Figure 6(a). When the loading amplitude reached 35 mm, the wood fiber between the mortise-tenon joints upwarped; when loaded to 80 mm, the timber made a continuous splitting sound. From Figure 6(b), the crevices parallel to the longitudinal direction are found to generate at the convex tenon. As loading continued, there existed apparent gaps amid mortises and tenons after the condition ending joint regained balance, as shown in Figure 6(c). When loaded to 120 mm, the mortise-tenon joints remained unfractured, but the test had to be stopped due to the excess pulling-out amount. Ban mortise-tenon joint JD-1b made a squeezing sound when loaded to 20 mm. When the loading amplitude reached 80 mm, the similar phenomenon to that with JD-1a was observed, with an observable pulling-out phenomenon; when the loading amplitude reached 110 mm, one convex tenon had completely fallen off the concave mortise. The test had to be stopped to prevent the convex tenon from falling off, as shown in Figure 6(e). Dovetail mortise-tenon joint JD-1c started to make a sound when loaded to 30 mm; when the loading amplitude reached 50 mm, the pulling-out phenomenon was rather severe. The rest of the experimental phenomena were similar to those with JD-1a. Due to the craftsmanship of both dovetail mortise-tenon joints, the actuator made a loud sound during its upward movement and a weak sound during its downward movement. When the loading amplitude reached 120 mm, no breakage had ever occurred to the mortise-tenon joints. The test was stopped when the cork on the upper end was extruded. The convex tenon was pulled out from the concave mortise, as shown in Figure 6(f).

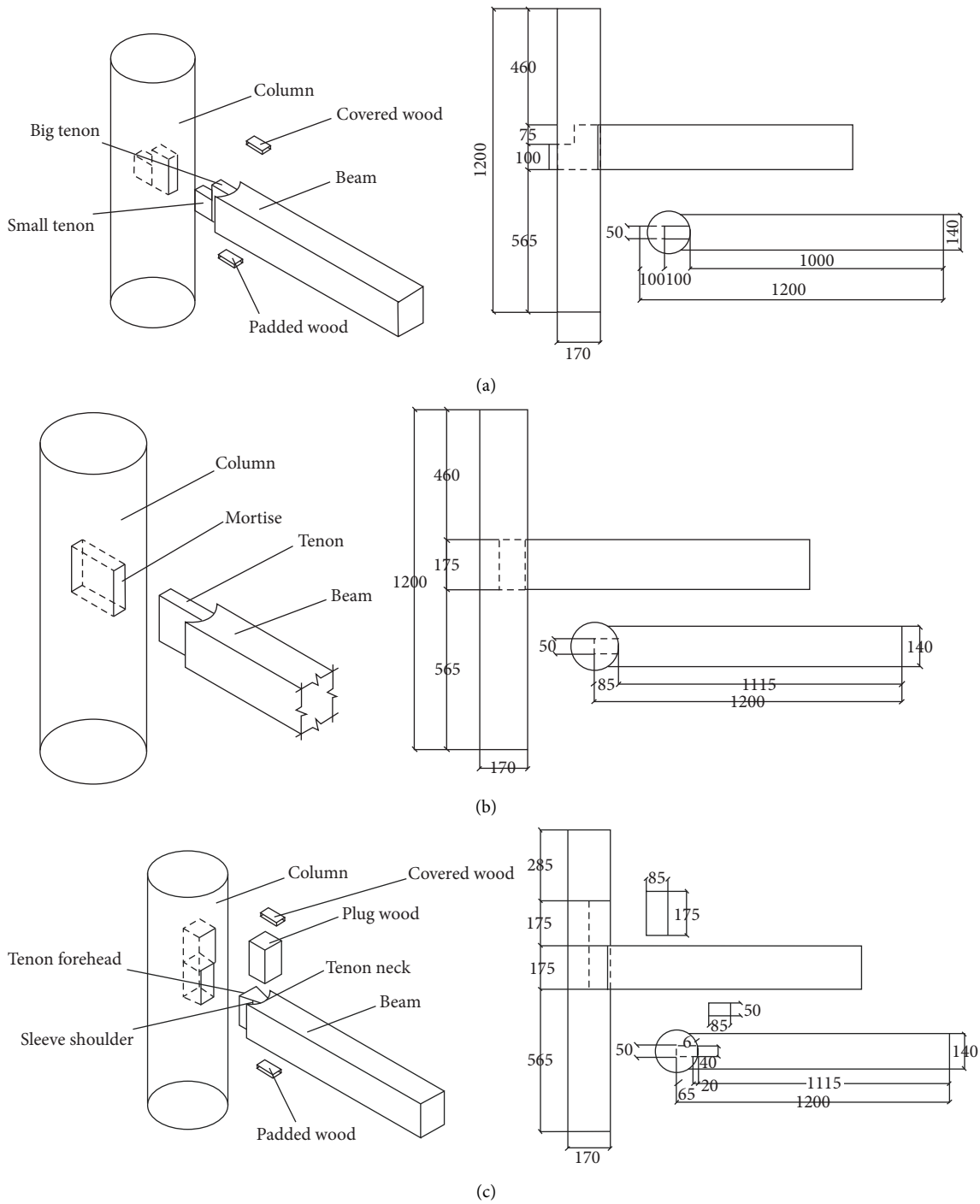

Figure 2: Diagram of mortise-tenon joints: (a) node diagram of Tou mortise-tenon joints. (b) Node diagram of ban mortise-tenon. (c) Node diagram of dovetail mortise-tenon joints.

3.2. Flat Steel Strip Reinforced Specimens. Tou mortise-tenon joint JD-2a made a sound at the maximum displacement due to friction and squeezing when the loading amplitude in the test reached 10 mm. With the increase in amplitude, the sound got louder, and the concave mortise became larger; when the loading amplitude reached 60 mm, the flat steel strip appeared significantly curved and deformed, and the convex tenon was ruptured, with one of its end losing the rotation ability and no longer displacing up and down with the beam; when the loading amplitude reached 120 mm, the actuator's maximum stroke, the flat steel strip experienced a significant deformation, and loading was stopped. Ban mortise-tenon joint JD-2b made a tapping sound just at the initial loading; when loaded to 30 mm, there appeared cracks in the convex tenon; when the loading stroke reached 50 mm, the concave mortise of the mortise-tenon joint

Table 1: Sizes of mortise-tenon.

Specimen no	Mortise-tenon type	Component name	Size (mm)
JD-1a JD-2a	Tou mortise-tenon joints	Height of the larger tenon	175
		Height of the smaller tenon	100
		Tenon width	50
		Length of the larger tenon	100
		Length of the smaller tenon	100
JD-1b JD-2b	Ban mortise-tenon joints	Tenon width	50
		Tenon height	175
		Tenon length	85
JD-1c JD-2c	Dovetail mortise-tenon joints	Width of tenon forehead	50
		Width of tenon neck	40
		Tenon height	175
		Tenon length	85
		Sleeve-shoulder length	20
		Sleeve-shoulder width	6

Table 2: Reinforcement method of joints.

Reinforcement method	Tou mortise-tenon joints	Ban mortise-tenon joints	Dovetail mortise-tenon joints
Unreinforced	JD-1a	JD-1b	JD-1c
Reinforced by flat steel strips (on the middle part of beams)	JD-2a	JD-2b	JD-2c

Table 3: Sizes of beams and columns.

Component name	Size (mm)	
Beam	Width	140
	Height	175
Column	Length	1200
	Diameter	170
	Length	1200

Table 4: Physical properties of wood.

Timber type	Air-dry density ($g \cdot cm^{-3}$)	Moisture content (%)
Hemlock (Tsuga chinensis)	0.452	13.02

Table 5: Mechanical properties of wood.

Timber type	$f_{c,L}$ (MPa)	$f_{c,T}$ (MPa)	$f_{c,R}$ (MPa)	f_b (MPa)	$E_{c,L}$ (MPa)	$E_{c,T}$ (MPa)	$E_{c,R}$ (MPa)
Hemlock (Tsuga chinensis)	35.13	3.51	3.71	56.77	7410	510	830

Note. $f_{c,L}$, $f_{c,T}$, $f_{c,R}$, and f_b correspond to the longitudinal chordwise, transverse chordwise, transverse radial compressive strengths, and bending strength of timber, respectively; $E_{c,L}$, $E_{c,T}$, and $E_{c,R}$ correspond to the longitudinal chordwise, transverse chordwise, and transverse radial compressive moduli of elasticity of timber, respectively.

cracked, and the sole timber originally placed above the convex tenon was extruded out; when the loading amplitude reached 80 mm, the flat steel strip appeared deformed, and the sound was augmented in loudness. The rest of the experimental phenomena were similar to those with JD-2a. Finally, the test ended upon loading to the actuator's maximum stroke. The loading phenomena of all joints are shown in Figure 7.

4. Results and Analyses

4.1. Hysteresis Curves of Joints. In this pseudo-static test, forward/backward loading coincided with the downward/upward movement of the actuator. The hysteresis curves of the six specimens are shown in Figure 8, where M is the bending moment with respect to the centroid of the mortise-tenon joint when the actuator was applying a vertical load on

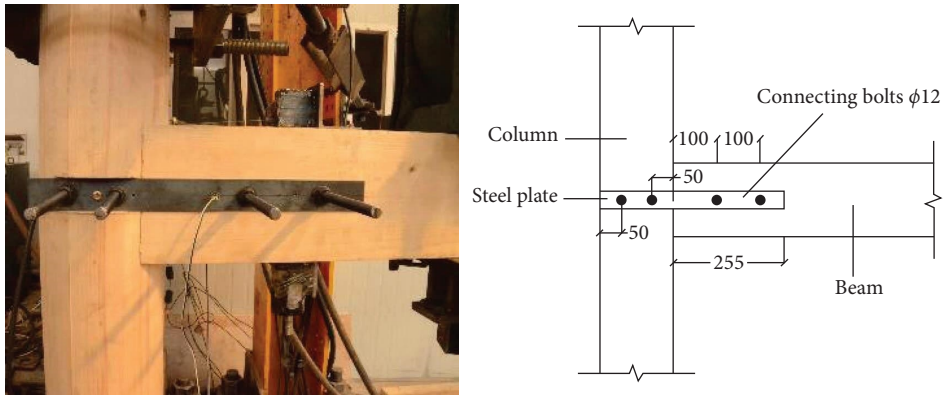

Figure 3: Diagram of specimens of reinforcement joints.

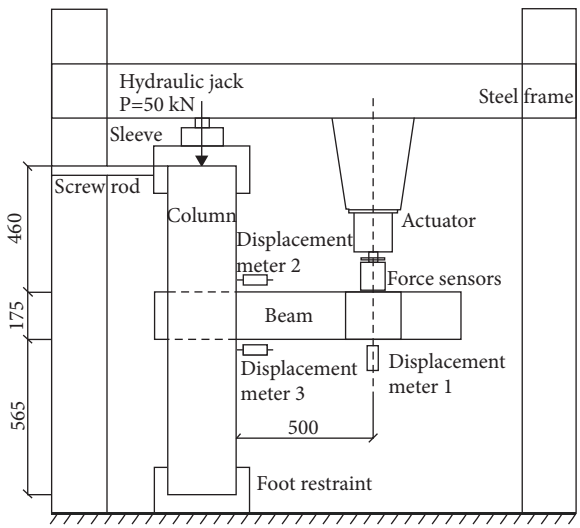

Figure 4: Experimental loading apparatus.

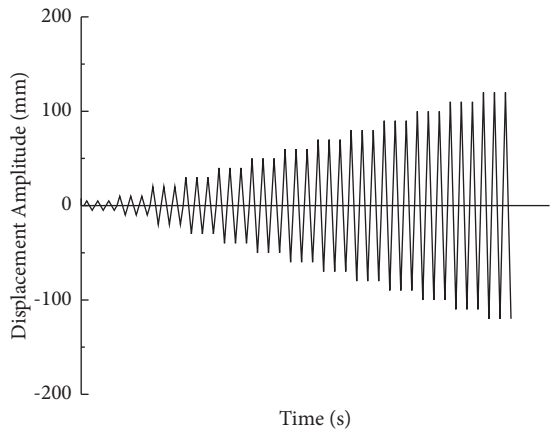

Figure 5: Loading program.

the beam end and θ is the turning angle of the beam. From the figure, the area enclosed by the hysteresis curve in whichever of the six experiments bears a positive correlation to loading amplitude. Among the curves, the hysteresis curves of both Tou mortise-tenon joints are plumper during backward loading than during forward loading. The greater bearing capacity and plumper feature manifested in the hysteresis curves are owing to the construction of Tou mortise-tenon joints such that the squeezing between the smaller convex tenon and the lower part of the concave mortise caused even severe friction and wedge pressure during backward loading. All the hysteresis curves in the graphs show an inverse Z-shape with rheostriction, that is, the bending moment M increased slowly while the turning angle θ increased rapidly at the initial stage of each condition, showing that there existed considerable amount of friction and slippage between the convex tenons and concave mortises in the test. Except for the joints with components destructed, the hysteresis areas in the first loop are all greater than those in the second and third loops under each condition. During later-stage unloading, the turning angle changed slightly while the bending moment decreased rapidly with obvious residual deformation due to the unrestorable plastic deformation generated from the squeezing between the convex tenon and the concave mortise during loading.

As shown in Figure 8, all the hysteresis curves of the unreinforced specimens present an inverse Z-shape. Among these specimens, the bending moment bearing capacity of JD-1a remained on the rising trend after its displacement turning angle reached 0.24 rad. Since the Ban tenon and dovetail tenon started to fracture after reaching a certain turning angle, the bearing capacity of Ban mortise-tenon joint JD-1b weakened significantly when the turning angle reached 0.13 rad; the bending moment of JD-1a reached 4.46 kN·m and remained on the increase when its turning angle reached 0.260 rad; the bending moment bearing capacity of dovetail mortise-tenon joint JD-1c started to decline after its turning angle reached 0.15 rad. It is shown that the capacity of Tou mortise-tenon joint JD-1a for bearing its bending moment is greater than those of Ban mortise-tenon joint JD-1b and dovetail mortise-tenon joint JD-1c in this test.

From Figure 9, the hysteresis curves of flat steel strip reinforced components show inverse Z-shapes in an early stage. Compared with the test on unreinforced specimens, the hysteresis curves of flat steel strip reinforced specimens

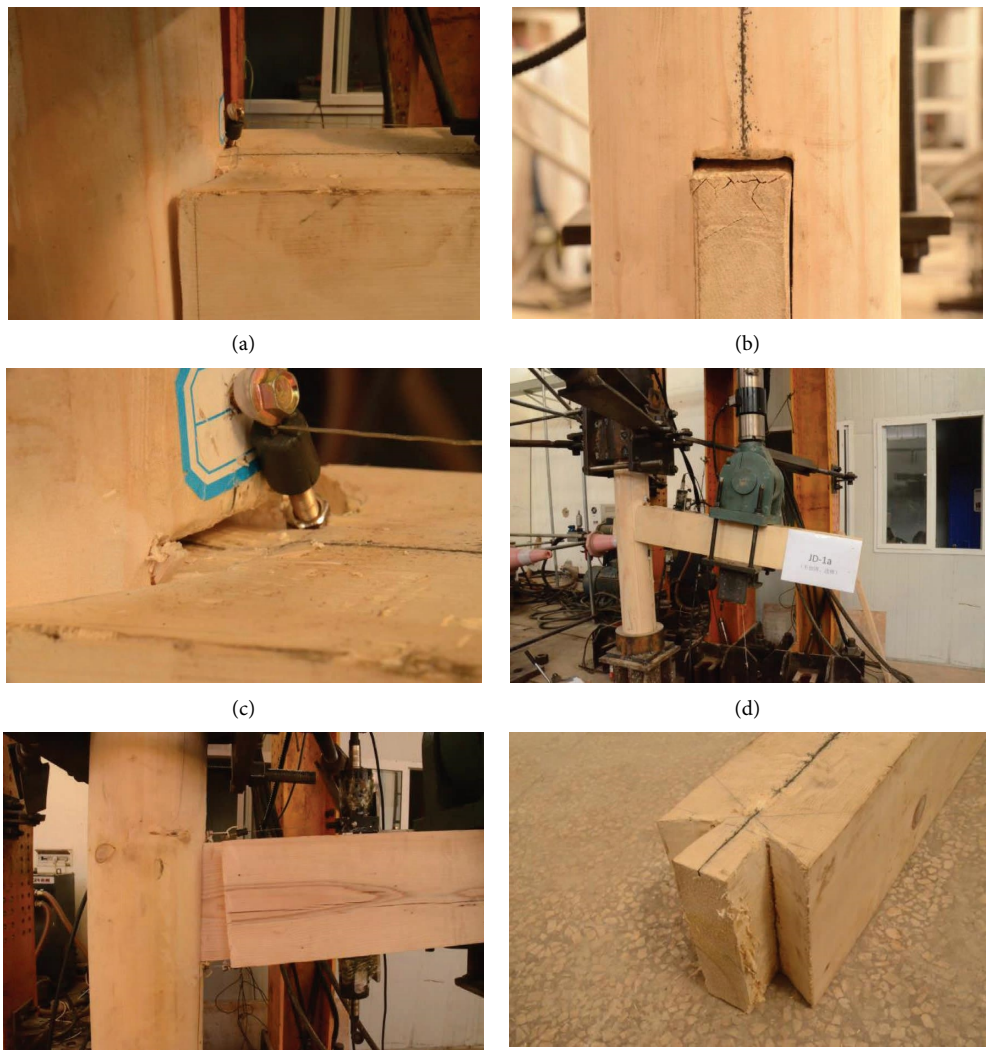

(a) (b) (c) (d) (e) (f)

Figure 6: Damage pattern of unreinforced specimens: (a) squeezing of a mortise-tenon joint. (b) Crevice in a convex tenon. (c) Flawing after squeezing. (d) Overlarge deformation of JD-1a. (e) Overlarge pulling-out amount of JD-1b. (f) Deformation of the convex tenon of JD-1c.

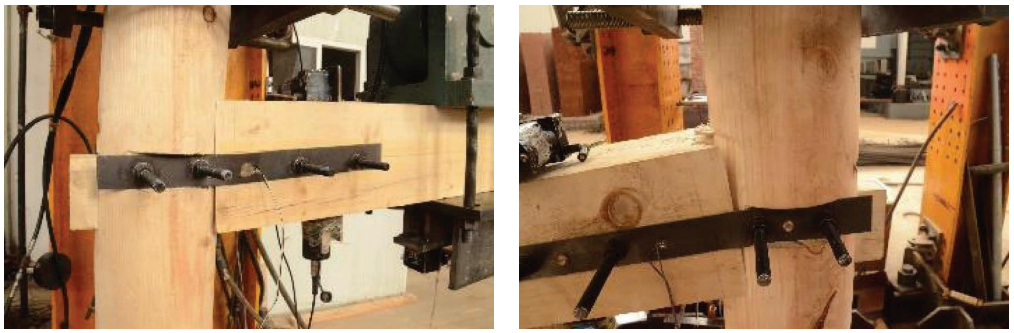

(a) (b)

Figure 7: Continued.

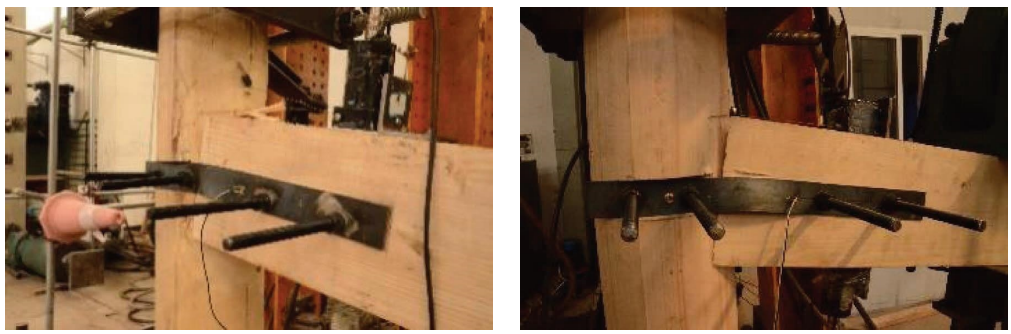

(c) (d)

Figure 7: Damage pattern of steel plate reinforced specimens: (a) deformation of the concave mortise of JD-2a. (b) Curving and deformation of the flat steel strip on JD-2a. (c) Abscission of wood timber of JD-2b. (d) Abscission of wood timber of JD-2c.

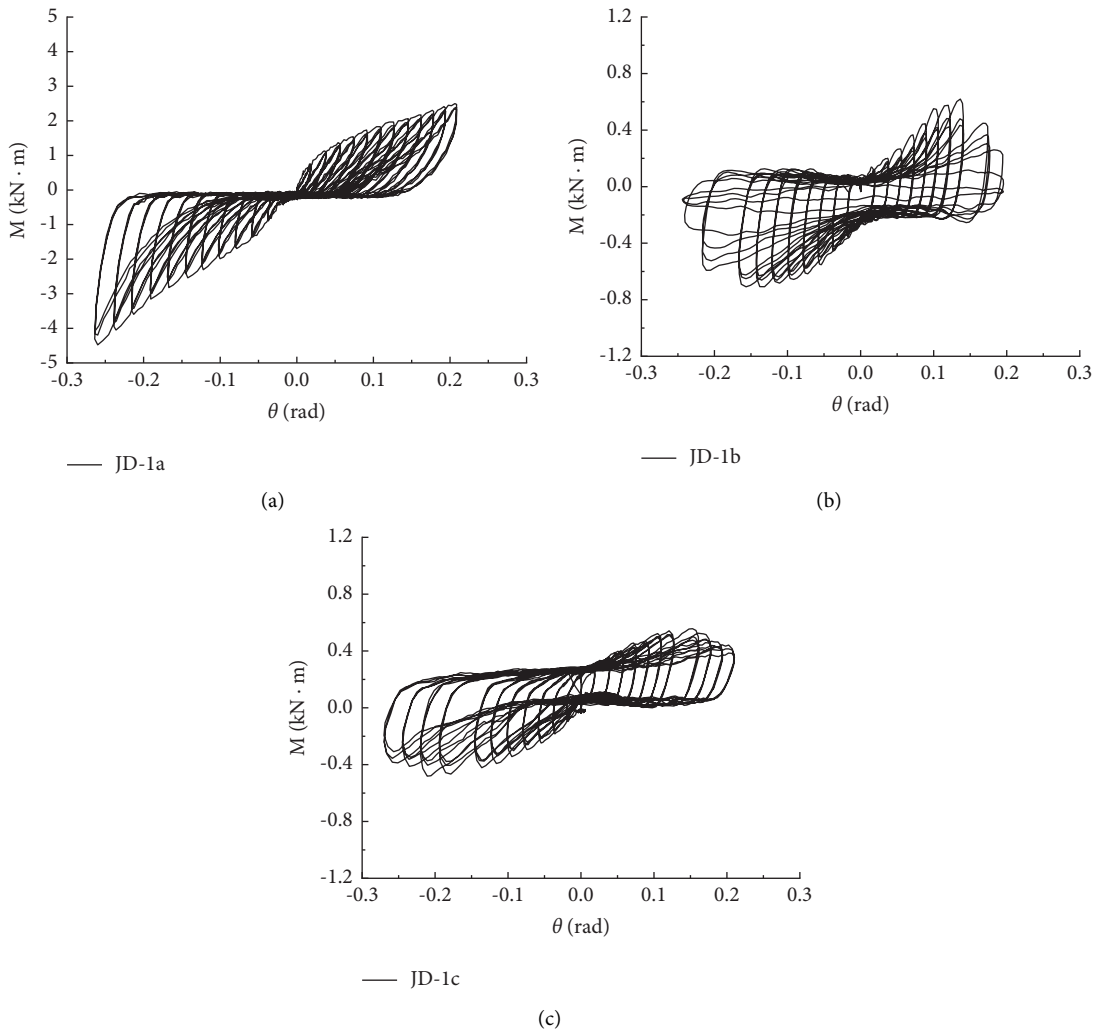

Figure 8: Moment-rotation hysteretic loops before reinforcement: (a) Tou mortise-tenon joints. (b) Ban mortise-tenon joints. (c) Dovetail mortise-tenon joints.

are plumper, effectively mitigating the rheostriction. This shows that the flat steel strips turn out effective in energy dissipation, reducing the slippage, and pulling-out phenomena of convex tenons. Due to the fracture of the convex tenon, the bending moment bearing capacity of Tou mortise-tenon joint JD-3a declined precipitously when the

turning angle of loading was −0.112 rad, but a certain bending moment bearing capacity was maintained and ever-rising in a later stage of loading, showing that the flat steel strips remained acting the role of energy dissipation after the convex tenon fractured. The bending moment bearing capacities of Ban mortise-tenon joint JD-1b and dovetail mortise-tenon joint JD-1c was rising steadily without declining during the loading process. On the above, installing flat steel strips can improve the energy-dissipating capacity, rigidity, and bearing capacity of joints.

4.2. Skeleton Curves of Joints. The skeleton curves of all mortise-tenon joints are shown in Figure 10, where subfigures (a), (b), and (c) are comparison graphs of the skeleton curves of Tou, Ban, and dovetail mortise-tenon joints in the reinforced and unreinforced states. From the graphs, the slope of the skeleton curve of the Tou mortise-tenon joint is greater than those of the other two forms of mortise-tenon joints in the unreinforced state at the initial stage of loading, showing that the Tou mortise-tenon joint has stronger bearing capacity and rigidity. In contrast, the bearing capacities of Ban and dovetail mortise-tenon joints increase slowly in the early stage due to the gaps amid their mortises and tenons.

The bearing capacities of the flat steel strip reinforced mortise-tenon joints rose to significant degrees in the order from the highest to the lowest: Ban mortise-tenon joint, dovetail mortise-tenon joint, and Tou mortise-tenon joint. The limit turning angles and ultimate bending moments of all mortise-tenon joints are shown in Table 6. At the ultimate turning angle, the bearing capacities of mortise-tenon joints improved insignificantly, even declining under backward loading due to the fracture of the convex tenons. During forward loading, the three mortise-tenon joints entered a yield stage when the turning angle reached 0.02 rad or so; during backward loading, except for the fracture of the convex tenon of Tou mortise-tenon joint, the bearing capacities of both Ban and dovetail mortise-tenon joints were on the rise without experiencing any descent stage. The flat steel strips had significant reinforcing effect on Ban and dovetail mortise-tenon joints by reinforcing them on the middle part, but the promotive effect was limited for the Tou mortise-tenon joint.

4.3. Energy Dissipation of Joints Analysis. The area E_d enclosed by the hysteresis curve of a mortise-tenon joint in each loop is used to reflect the energy-dissipating capacity of that joint. The higher the value of E_d, the stronger the energy-dissipating capacity; otherwise, the weaker. Figure 11 shows the comparison in energy dissipation between the reinforced and unreinforced cases of three mortise-tenon joints. The energy-dissipating capacity of joints is significantly promoted in the reinforced case than in the unreinforced case. Among the joints, the value of E_d of Tou mortise-tenon joint JD-2a increased by 12.07% over JD-1a when the turning angle reached 0.22 rad, the value of E_d of Ban mortise-tenon joint JD-2b increased by 130.82% over JD-1b when the turning angle reached 0.2 rad, and the value of E_d of dovetail mortise-tenon joint JD-2c increased by 198.52% over JD-1c when the turning angle reached 0.22 rad. Except for the fracture of the convex tenon of the Tou mortise-tenon joint, the energy-dissipating capacities of both the other flat steel strip reinforced joints have increased. The growth rates of energy-dissipating capacities of the unreinforced joints declined in a later stage of loading. The energy-dissipating performances of the reinforced joints remained on a rising trend.

4.4. Rigidity Degeneration of Joints Analysis. Rigidity degeneration of the joint is a phenomenon that the joint's rigidity declines with the increase of loading control displacement and loop count. To be evaluated more accurately, the rigidity of mortise-tenon joints is usually represented by secant rigidity K_i as shown in the following formula:

$$K_i = \frac{\left|+M_i\right| + \left|-M_i\right|}{\left|+\theta_i\right| + \left|-\theta_i\right|}, \quad (1)$$

where M_i is the peak value of bending moment at the i^{th} grade of the turning angle during the first loop; θ_i is the turning angle corresponding to M_i.

The secant rigidity K_i in Figure 12 is determined by formula (1). From the figure, the rigidity degeneration curves of the reinforced and unreinforced joints have similar trends: the greater the amplitude the smaller the rigidity. The rigidity of Ban mortise-tenon joints declined after the convex tenons fractured, even to below that of unreinforced specimen JD-1a; the initial rigidity of the Ban mortise-tenon joint JD-1b was larger but slumped subsequently. The rigidity dropped rapidly because there existed gaps amid the mortise and tenon, which were artificially filled with a cork, and the cork was squeezed out due to the compressional deformation between the mortise and tenon after the turning angle of loading reached 0.05 rad. The rigidity of the reinforced dovetail mortise-tenon joint was always greater than that of the unreinforced joint. With the increase of loading loop count, the rigidity of the joints declined, and the performance degraded.

Table 7 estimates the initial rigidities and secant rigidities of all test specimens of joints, where the initial rigidity represents the ratio of yielding moment to yielded turning angle. The values of yielding moment and yielded turning angle are derived from Figure 10. According to the secant rigidities determined by formula (1), the mean and covariance of them are aggregated.

4.5. Energy Dissipation Analysis of Joints. Utilizing the hysteresis curves under low-frequency cyclic loading, one can analyze how the test specimens absorb and dissipate energy at the nonelastic deformation stage. The energy-dissipating capacity of components is usually measured by the equivalent viscous damping coefficient h_e. The greater the value of h_e, the stronger the energy-dissipating capacity of joints. According to Figure 13, the equivalent viscous damping coefficient is calculated by formula (2). The equivalent viscous damping coefficients of all test specimens are shown in Figure 14.

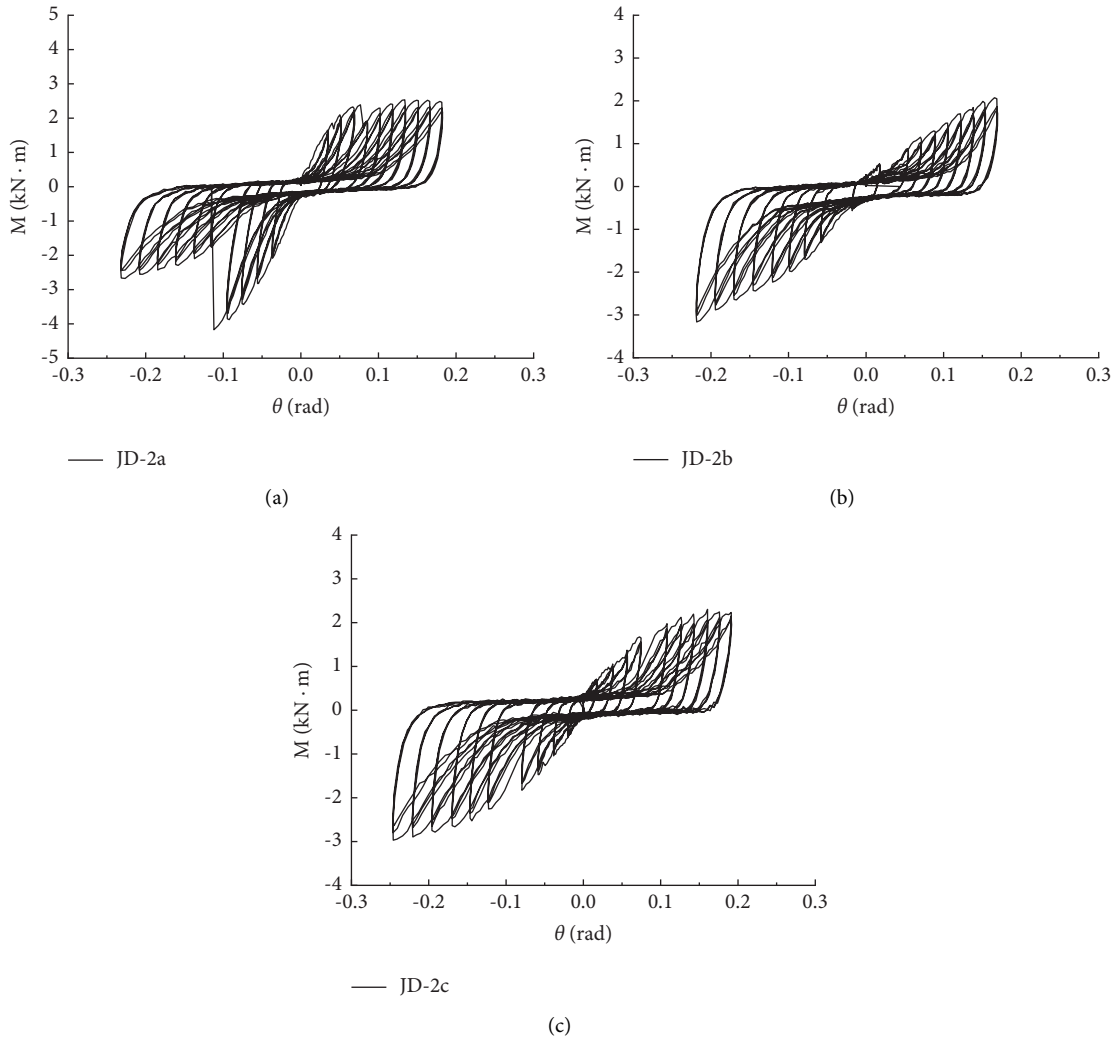

Figure 9: Moment-rotation hysteretic loops after reinforcement with steel plate: (a) Tou mortise-tenon joints. (b) Ban mortise-tenon joints. (c) Dovetail mortise-tenon joints.

$$h_e = \frac{1}{2\pi} \times \frac{S_{ABCD}}{S_{\Delta OAE} + S_{\Delta OCF}}, \tag{2}$$

where h_e is the equivalent viscous damping coefficient of joints; S_{ABCD} is the area enclosed by the hysteresis curve in the figure; $S_{\Delta OAE} + S_{\Delta OCF}$ is the area of the triangle corresponding to the peak points in the hysteresis loop.

It can be seen that, with the increase of the turning angle, the equivalent viscous damping coefficient declines rapidly at the initial stage and gradually gently at the later stage. The energy-dissipating capacity of Tou tenons is weak in both the reinforced and unreinforced states; there is little difference between the energy-dissipating capacities of Ban tenons and dovetail tenons. For more intuitive analysis of the energy-dissipating capacity of all test specimens of joints, the sum of the areas of the hysteresis loops under each operating condition is adopted to denote the cumulative energy dissipation of joints, as shown in Table 6. From the table, the energy-dissipating capacity of all joints has improved dramatically after installing the damper, reflecting the superiority of flat steel strip reinforced joints in energy dissipation.

4.6. Theoretical Calculation of the Load-Carrying Capacity of Reinforced Nodes. The overall load-bearing capacity of the reinforced node is provided by both the timber and the flat steel strip and can be reflected in equation (3) for the overall load-bearing capacity:

$$M_t = M_w + M_s, \tag{3}$$

where M_t is overall load-bearing capacity of reinforced nodes, M_w is load-bearing capacity provided by wood, and M_s is load-bearing capacity provided by flat steel strips.

M_w is summarized in Table 8 based on Gao et al.'s study [36], where P_t and P_b are the embedding pressure at the outer end of the tenon; $l_{c,t,b}$ is the length, height, and width of the pressurized area, respectively; $t_{c,t,b}$ is the length, height, and width of the tenon, respectively; δ is the inlay depth of

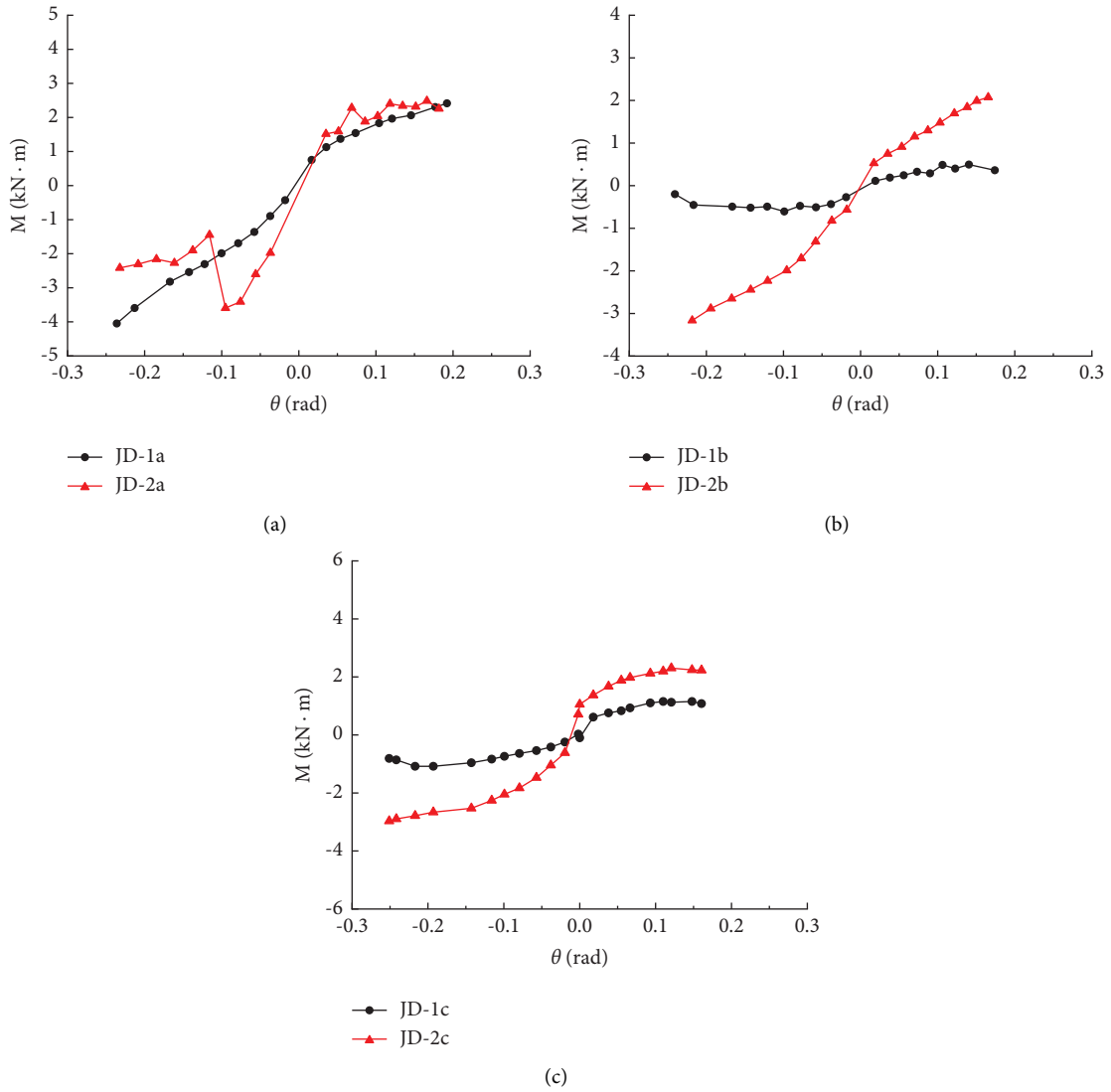

FIGURE 10: Moment-rotation backbone curves of joint after reinforcement with steel plate: (a) Tou mortise-tenon joints. (b) Ban mortise-tenon joints. (c) Dovetail mortise-tenon joints.

the wood; δ_y is the yield displacement of the wood; μ is the coefficient of friction between the wood.

M_s is the bearing capacity provided by the lateral bending of the flat steel strip, due to the flat steel strip width to thickness ratio is too large, in the process of the proposed static test is prone to out-of-plane instability. Also, since the flat steel strip is bolted to the wood, it is difficult to accurately assess the force pattern of the flat steel strip, so Origin was used to fit the skeleton curve to derive the relationship between M_s and the angle of rotation, where the skeleton curve used for the fit is the skeleton curve of the reinforced nodes minus the skeleton curve of the unreinforced nodes in Figure 10, and the result obtained is shown in Figure 15. The fitted equation for the moment load capacity of the flat steel strip versus the angle of rotation is shown in Table 9.

5. FEA

5.1. Modeling. Since there exists certain room for optimization in aseismic performance of mortise-tenon joints reinforced on the middle part by the flat steel strips, the finite element software ABAQUS [37] was adopted for simulation and comparison of the abovementioned tests and to change the position of reinforcement with the flat steel strips in the model, so as to achieve the result of upgrading the performance of the joints.

Table 6: Comparison of nodal ultimate bending moments.

Mortise-tenon type	Specimen no	Reinforcement method	Direction	Ultimate corner (rad)	Ultimate bending moment (kN·m)	Boost ratio
Tou mortise-tenon joints	JD-1a	Unreinforced	Forward	0.2064	2.4988	4% improvement in forward direction, 20% reduction in backward direction
			Backward	0.25996	4.47745	
	JD-2a	Reinforced	Forward	0.16608	2.58665	
			Backward	0.09506	3.5942	
Ban mortise-tenon joints	JD-1b	Unreinforced	Forward	0.13654	1.3739	51% improvement in forward direction, 111% improvement in backward direction
			Backward	0.14226	1.4966	
	JD-2b	Reinforced	Forward	0.16554	2.07425	
			Backward	0.21836	3.16485	
Dovetail mortise-tenon joints	JD-1c	Unreinforced	Forward	0.1103	0.43915	425% improvement in forward direction, 934% improvement in backward direction
			Backward	0.14564	0.28705	
	JD-2c	Reinforced	Forward	0.16058	2.3047	
			Backward	0.24588	2.9686	

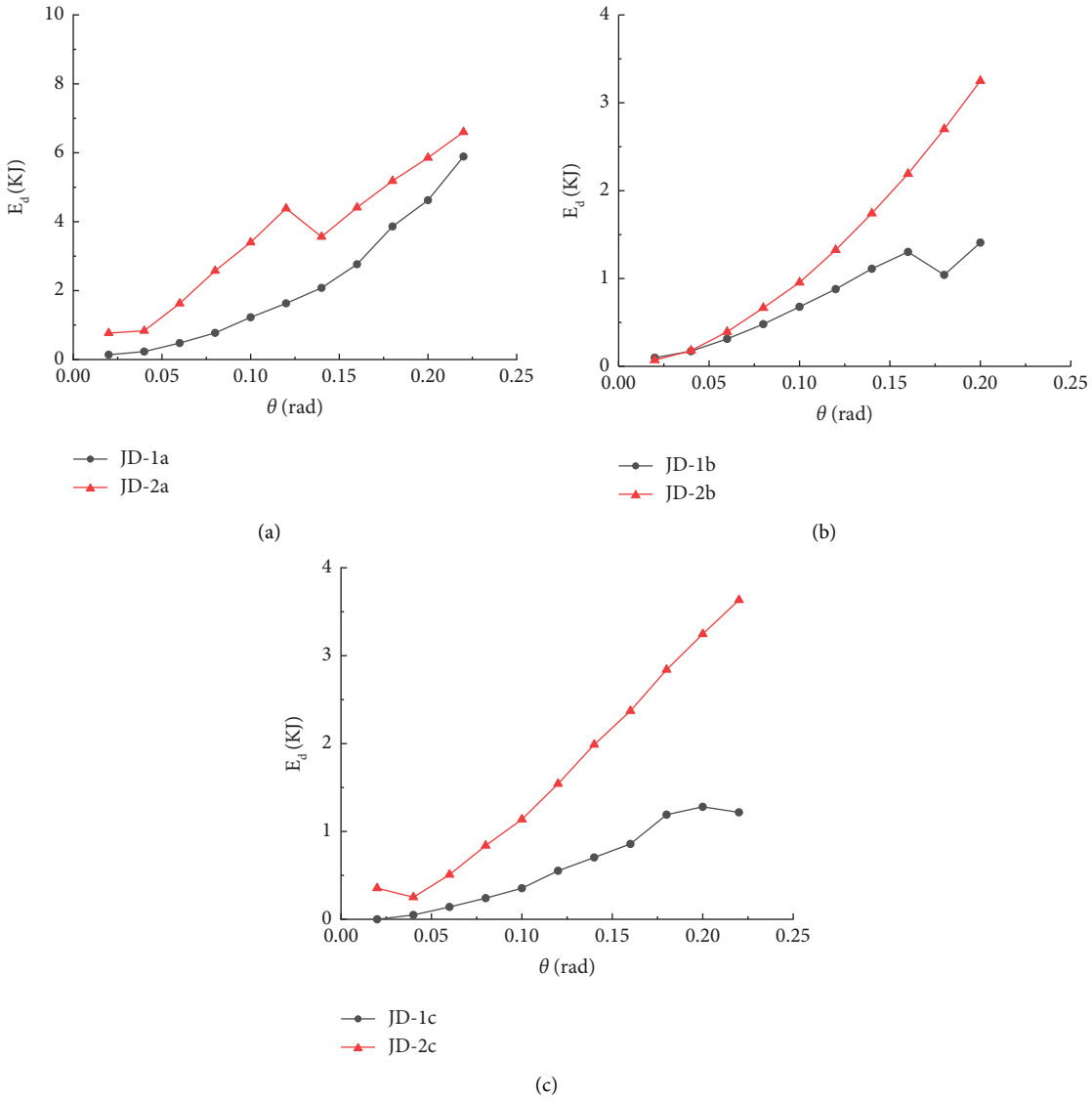

Figure 11: Hysteresis curve energy consumption area comparison: (a) Tou mortise-tenon joints. (b) Ban mortise-tenon joints. (c) Dovetail mortise-tenon joint.

In this paper, a modeling analysis was conducted on the stress performance of the mortise-tenon joints using ABAQUS, as shown in Figure 16. The timber was simplified as an orthogonal anisotropic material. An eight-joint hexahedral linear unit C3D8R was adopted in modeling. All engineering constants at the elastic stage Engineering Constants in ABAQUS software were defined according to Table 7. The initial yield ratios of all items of the timber were defined using the *potential* function at the plastic stage [38], to simulate the stress performance of all items of the timber at this stage, where the following settings were made: $R11 = 1$, $R22 = 0.124$, $R33 = 0.111$, $R12 = 0.326$, $R13 = 0.326$, and $R23 = 0.326$; column gridding size = 15 mm, beam gridding size = 12 mm, and flat steel strip gridding size = 12 mm; interunit contact was set as surface-to-surface contact; the longitudinal direction coincided with the principal surface, and the transverse direction coincided with the subordinate surface; the form of interaction between flat steel strip and timber was binding.

The reinforced joints are shown in Figure 17, where the flat steel strip material is Q235 steel. The sizes when the flat steel strips were reinforcing on the middle part of the beams are shown in Figure 2. To reinforce a beam on the upper and lower ends, an originally 40 mm wide flat steel strip was cut into two 20 mm wide flat steel strips, which were then placed separately on the top and bottom of the mortise-tenon joint.

Reference points were set and coupled at the top, bottom, and 500 mm away from the end of a column. A 10 kN vertical centralized load was applied on the upper end of the wooden column to simulate the roofing load; a fixed constraint was applied on the bottom of the column; a displacement constraint of the amplitude in the pseudo-static test was added 500 mm away from the end of the column. Hard contact was adopted in the normal direction, whereas

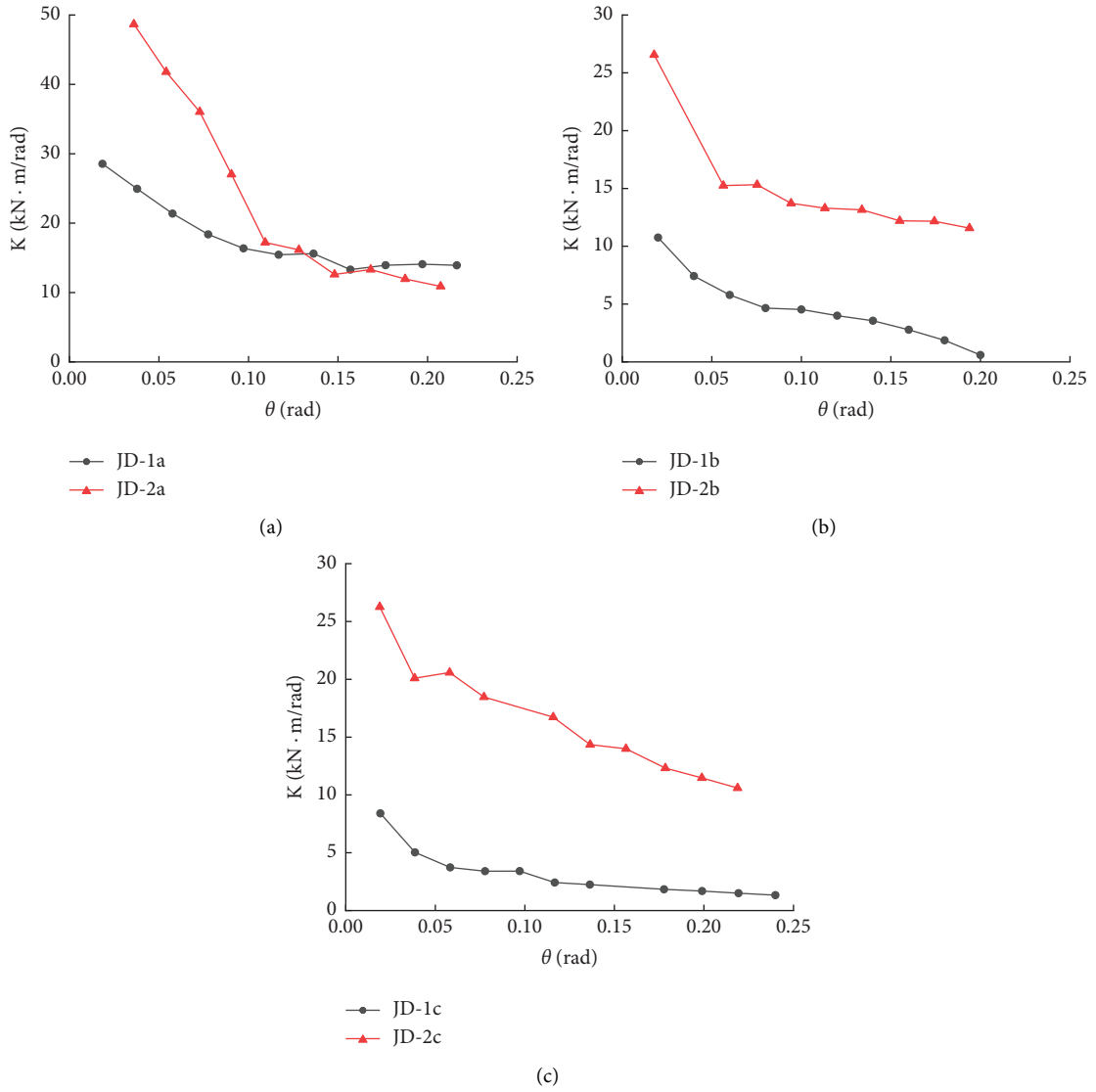

Figure 12: Curves of rigidity degradation: (a) Tou mortise-tenon joints. (b) Ban mortise-tenon joints. (c) Dovetail mortise-tenon joints.

Table 7: Comparison of stiffness before and after reinforcement.

Mortise-tenon type	Specimen no	Reinforcement method	Initial stiffness	Average secant stiffness	Secant stiffness covariance, Cov (JD-1X, JD-2X), $X = a, b, c$
Tou mortise-tenon joints	JD-1a	Unreinforced	34.44	4.01	63.55
	JD-2a	Reinforced	126.74	11.86	
Ban mortise-tenon joints	JD-1b	Unreinforced	35.14	2.04	10.18
	JD-2b	Reinforced	81.07	2.83	
Dovetail mortise-tenon joints	JD-1c	Unreinforced	18.37	1.47	8.75
	JD-2c	Reinforced	36.08	3.94	

penalty friction was adopted in the tangent direction, to the interaction between mortises and tenons. According to the existing studies, the coefficient of friction between timbers was taken as 0.4.

5.2. Comparisons between FEA and Experimental Results

5.2.1. Comparison between Hysteresis Curves. Figures 18 and 19 compare the hysteresis curves through test and finite

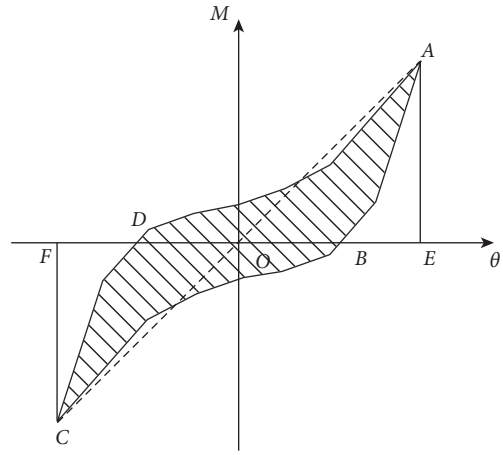

Figure 13: Computing sketch of viscous damping ratio.

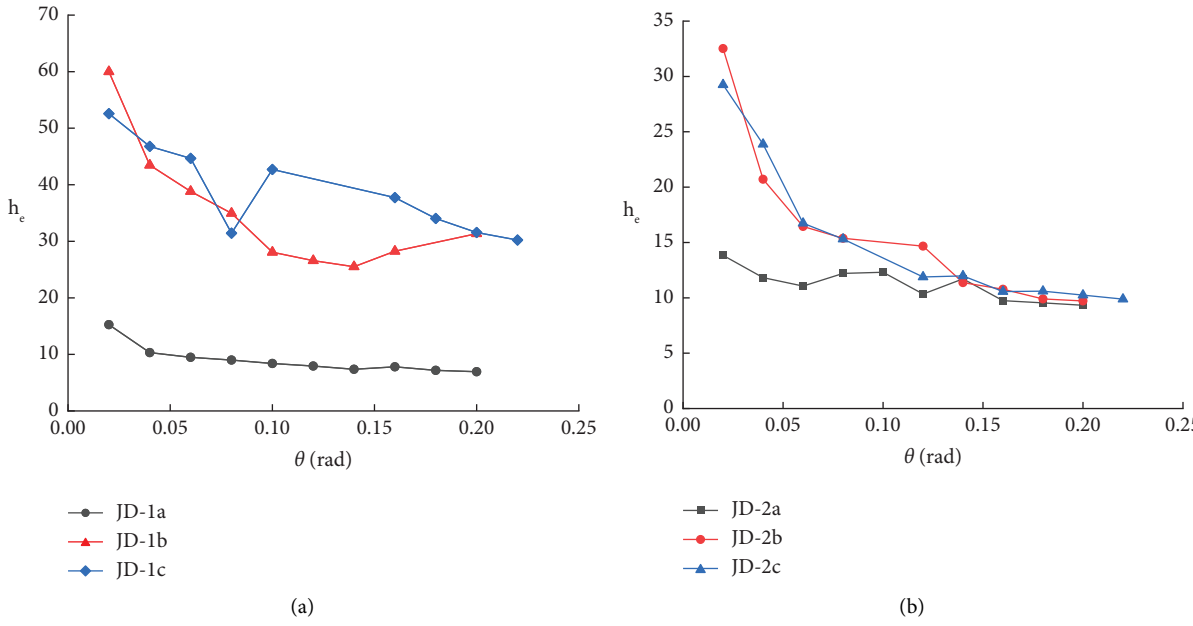

Figure 14: Viscous damping of continuous tenon joint: (a) unreinforced nodes. (b) Reinforcement nodes.

element simulation among three types of mortise-tenon joints under the unreinforced condition and the reinforced condition with flat steel strips through the beams. Due to the slippage of the actuators of Ban and Tou mortise-tenon joints in the unreinforced state during the test, the test curves are not symmetrical about the 0 point because the initial displacement was not zeroed after each set of conditions. As a result, there exist certain differences between the test curves and the simulation curves, as shown in Figures 16(b)-16(c). From the graphs, the hysteresis curves through finite element simulation show generally consistent trends, i.e., an inverse Z-shape, with the test curves for the models of Tou and dovetail mortise-tenon joints. From Figure 16(b), there exist certain differences between the hysteresis curve through finite element simulation and the test curve for Ban mortise-tenon joints in the unreinforced state for the following reasons: (1) there existed gaps amid mortises and tenons of Ban mortise-tenon joints during the test, while it was difficult to represent the real gaps during the simulation; (2) the actuators limited the pulling-out to a certain extent during the test, while the beam activity was free-directional during the numerical simulation, so that the pulling-out phenomenon was observable. Hence, there exist differences between the hysteresis curves. (3) The test timber was broken, making it difficult to restore the condition of the real timber by numerical simulation.

5.2.2. Comparison between Skeleton Curves. Figures 20 and 21 compare the skeleton curves through test and finite element simulation among three types of mortise-tenon joints under the unreinforced condition and the reinforced condition with flat steel strips through the beams. From the graphs, all simulation values are greater than the test values.

Table 8: Different nodes M_w relationship model.

Mortise-tenon type	Stage		Formula
Tou mortise-tenon	Flexibility	Clockwise	$M = P_t(t_{l1} - l_{c,t}/3) + P_b(t_{l2} - l_{c,t}/3) + F_b t_{d1}$ $P_t = E_{90}/t_{d1}(1/2\,l_{c,t}^2 t_w + 0.6 l_{c,t} t_w t_{d1})\theta$; $P_b = E_{90}/t_{d2}(1/2 l_{c,t}^2 t_w + 0.6 l_{c,t} t_w t_{d2})\theta$
		Counterclockwise	$M = P_b{}' t_{l1} + P_t{}' t_{l2} + F_b{}' t_{d1} + F_t'(t_{d2} - t_{d1})$ $P_t{}' = E_{90}/t_{d1}(1/2 l'^2_{c,t} t_w + 0.6 l_{c,t}' t_w t_{d1})\theta$; $P_b' = E_{90}/t_{d2}(1/2 l'^2_{c,t} t_w + 0.6 l_{c,t}' t_w t_{d2})\theta$ $F_t' = \mu P_t'(1 + \nu_{23})$; $F_b' = \mu P_b'(1 + \nu_{23})$
	Plasticity	Clockwise	$M_p = M_{\mathrm{pR}} + M_{pRF}$ $M_{\mathrm{pR}} = E_{90}\delta_y t_w/2t_{d1}(\delta - \delta_y/\theta + t_{d1}/1.5\ln\delta_y/\delta + l_{ct} + 1.5t_{d1})(t_{l1} - l_{ct}/3) +$ $E_{90}\delta_y t_w/2t_{d2}(\delta - \delta_y/\theta + t_{d2}/1.5\ln\delta_y/\delta + l_{cb} + 1.5t_{d2})(t_{l2} - l_{cb}/3)$ $M_{pRF} = E_{90}\delta_y t_w t_{d1}\mu(1 + \nu_{23})/2t_{d2}(\delta - \delta_y/\theta + t_{d2}/1.5\ln\delta_y/\delta + l_{cb} + 1.5t_{d2})$
		Counterclockwise	$M_p{}' = M_{\mathrm{pR}}{}' + M_{pRF}{}'$ $M_{\mathrm{pR}}{}' = E_{90}\delta_y t_w/2t_{d1}(\delta - \delta_y/\theta + t_{d1}/1.5\ln\delta_y/\delta + l_{cb}' + 1.5t_{d1})(t_{l1} - l_{cb}'/3) +$ $E_{90}\delta_y t_w/2t_{d2}(\delta - \delta_y/\theta + t_{d2}/1.5\ln\delta_y/\delta + l_{ct}' + 1.5t_{d2})(t_{l2} - l_{ct}'/3)$ $M_{pRF}{}' = E_{90}\delta_y t_w t_{d1}\mu(1 + \nu_{23})/2t_{d2}(\delta - \delta_y/\theta + t_{d1}/1.5\ln\delta_y/\delta + l_{cb}' + 1.5t_{d1}) +$ $E_{90}\delta_y t_w t_{d1}\mu(1 + \nu_{23})/2t_{d2}(\delta - \delta_y/\theta + t_{d2}/1.5\ln\delta_y/\delta + l_{ct}' + 1.5t_{d2})(t_{d2} - t_{d1})$
Ban mortise-tenon	Flexibility		$M = E_{90}/t_d l_u(l_c^2 t_w + 0.6 l_c t_w t_d)\theta + E_{90}\mu(1 + \nu_{23})(0.5 l_c^2 t_w + 0.3 l_c t_w t_d)\theta$
	Plasticity		$M_p = 2P_p l_u + \mu(1 + \nu_{23}) t_d P_p$ $P_p = E_{90}\delta_y t_w/2t_d[(\delta - \delta_y/\theta + t_d/2\ln\delta_y/\delta) + (l_c + 1.5t_d)]$
Dovetail mortise-tenon	Flexibility		$M = E_{90}/t_d(t_l/2 - l_c/3)(l_c^2 t_w + 0.6 l_c t_w t_d)\theta + E_{90}\mu(1 + \nu_{23})/2(l_c^2 t_w + 0.6 l_c t_w t_d)\theta$
	Plasticity		$M_p = 2P_p l_u + \mu(1 + \nu_{23}) t_d P_p + \mu P_N(t_d/2 - h'/3)$ $P_p = E_{90}\delta_y t_w/2t_d[(\delta - \delta_y/\theta + t_d/2\ln\delta_y/\delta) + (l_c + 1.5t_d)]$

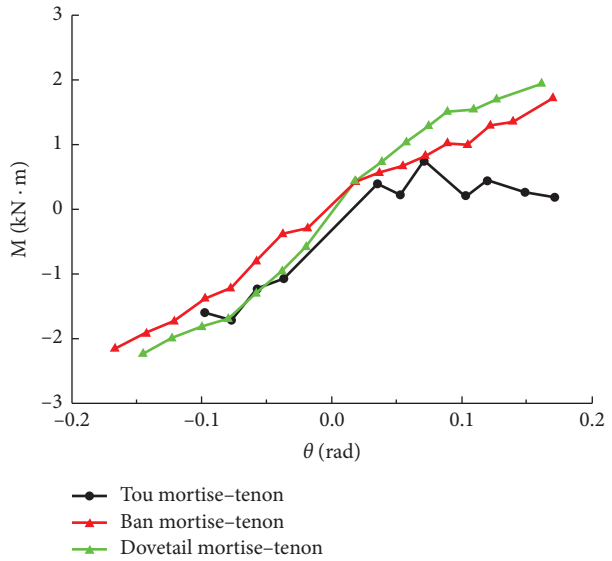

Figure 15: Load-bearing skeleton curves of flat steel strips on different mortise and tenon nodes.

Table 9: Different nodes M_s relationship model.

Mortise-tenon type	Formula
Tou mortise-tenon	$M_S = 14.28199\theta - 29.2174\theta^2 - 238.31645\theta^3 - 0.35675$
Ban mortise-tenon	$M_S = 11.76797\theta - 6.52434\theta^2 - 0.04481$
Dovetail mortise-tenon	$M_S = 15.82531\theta - 10.02519\theta^2 - 0.06092$

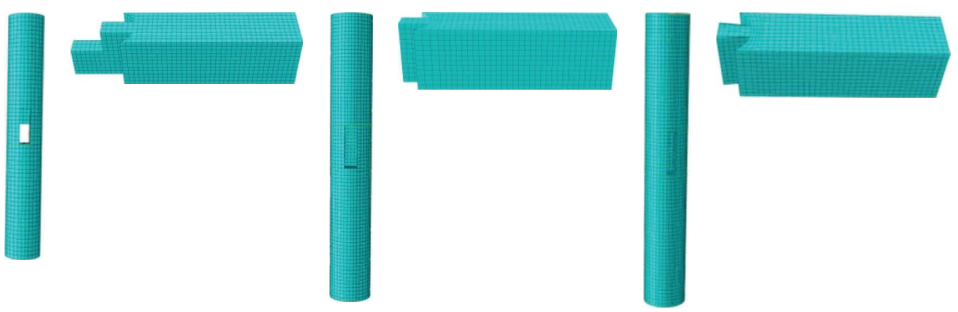

Figure 16: Element meshing: (a) Tou mortise-tenon column. (b) Tou mortise-tenon beam. (c) Ban mortise-tenon column. (d) Ban mortise-tenon beam. (e) Dovetail mortise-tenon column. (f) Dovetail mortise-tenon beam.

Overall, finite element simulation and test values follow roughly the same trends and are highly coincident. The finite element simulation data are slightly greater than the test data for the following reasons: (1) the numerical simulation targeted the ideal performance of the timber, whereas the timer performance during the test was discrete; (2) there existed the gaps amid mortises and tenons during the test, which were hard to represent and simulate during the finite element simulation. From the eigenvalues of mortise-tenon curves in Table 10, it can be seen that, except for the Ban tenon joints, the errors between the numerical simulation results and test average values are all within a controllable range, suggesting that the numerical simulation of mortise-tenon joints in this paper can be adopted for force analysis of wooden structures.

5.3. Comparisons through FEA between Different Positions of Reinforcement with the Flat Steel Strips

5.3.1. Comparison between Hysteresis Curves. Figure 22 compares the hysteresis curves for different positions where the mortise-tenon joints were reinforced by the flat steel strips. From the graphs, the hysteresis curves for the middle part of beams where the joints were reinforced by the flat steel strips render inverse Z-shapes. Compared with those for the middle part where the mortise-tenon joints

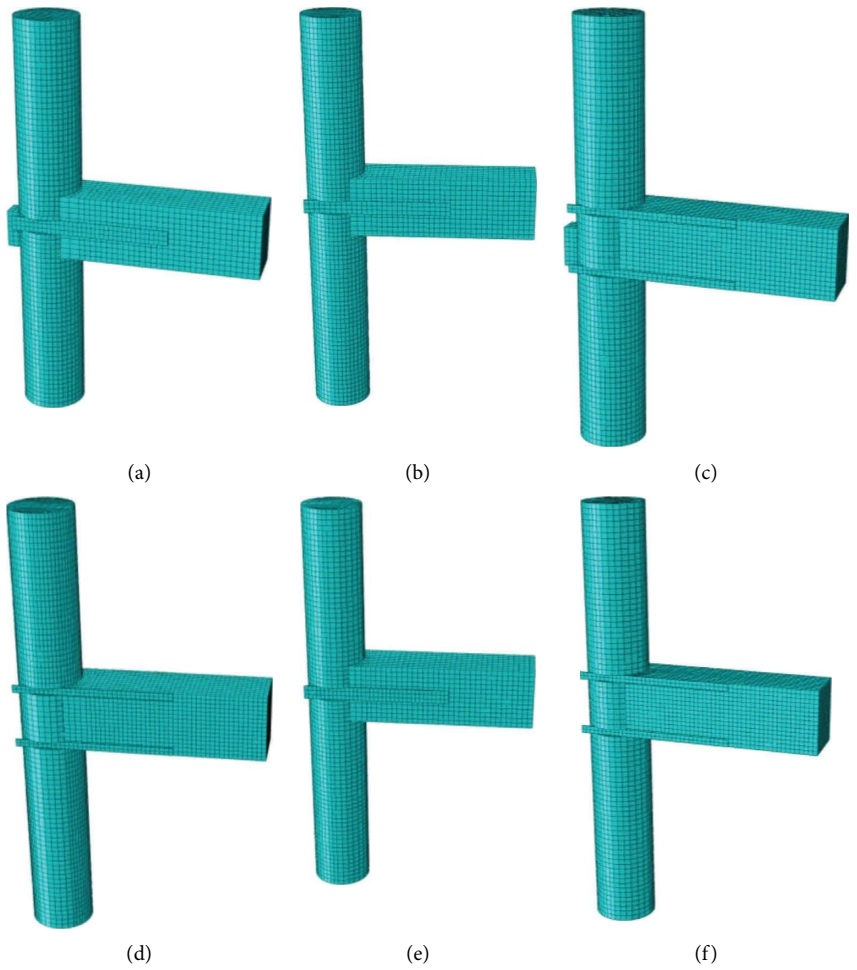

Figure 17: Finite element model of different steel plate reinforcement positions: (a) JD-2a model. (b) JD-2b model. (c) JD-3a model. (d) JD-3b model. (e) JD-2c model. (f) JD-3c model.

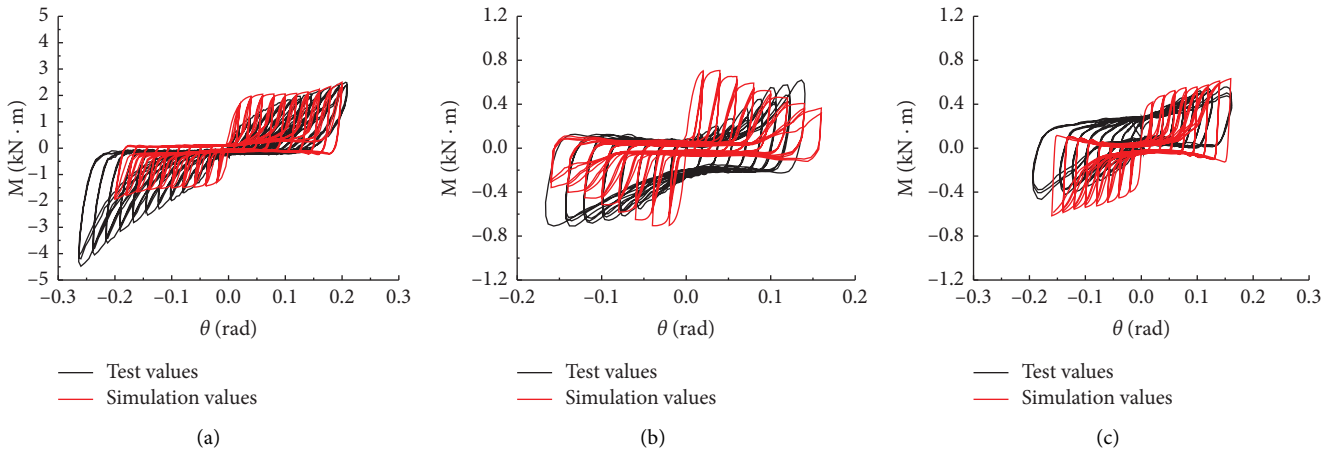

Figure 18: Comparison of moment-rotation hysteretic loops of unreinforced joints: (a) Tou mortise-tenon joints. (b) Ban mortise-tenon joints. (c) Dovetail mortise-tenon joints.

were reinforced by the flat steel strips, the hysteresis curves for both the upper and lower ends where the mortise-tenon joints were reinforced by the flat steel strips are obviously plumper with significantly reduced rheostriction and increased hysteresis areas, indicating that the energy dissipation and seismic mitigation effects were better when the

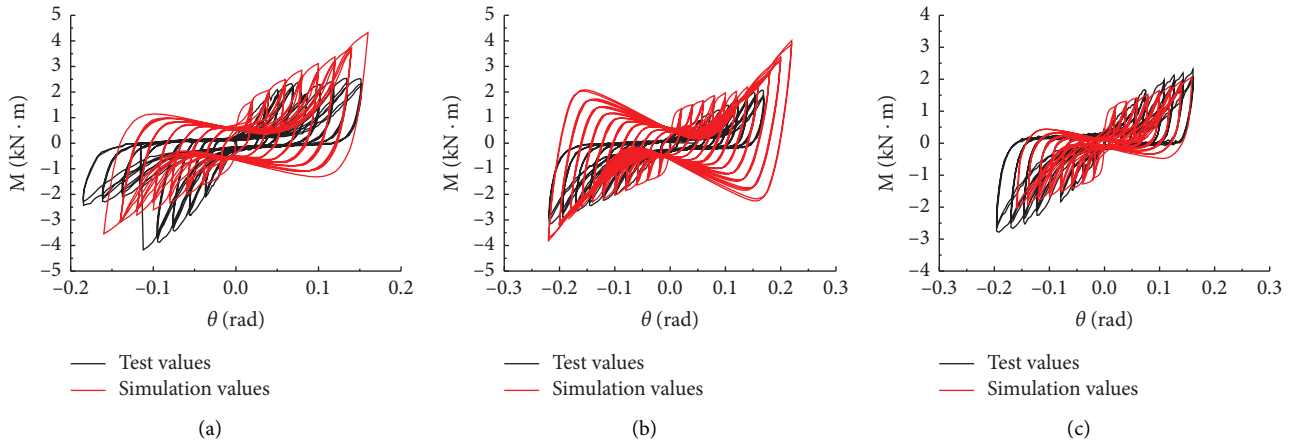

Figure 19: Comparison of moment-rotation hysteretic loops of middle joints of steel plate reinforced: (a) Tou mortise-tenon joints. (b) Ban mortise-tenon joints. (c) Dovetail mortise-tenon joints.

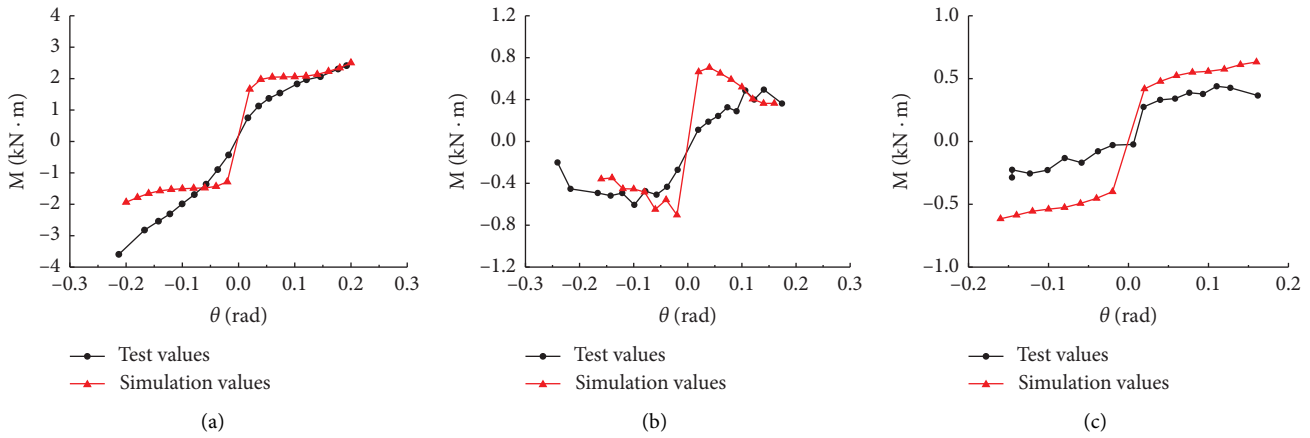

Figure 20: Comparison of moment-rotation backbone curves of unreinforced joints: (a) Tou mortise-tenon joints. (b) Ban mortise-tenon joints. (c) Dovetail mortise-tenon joints.

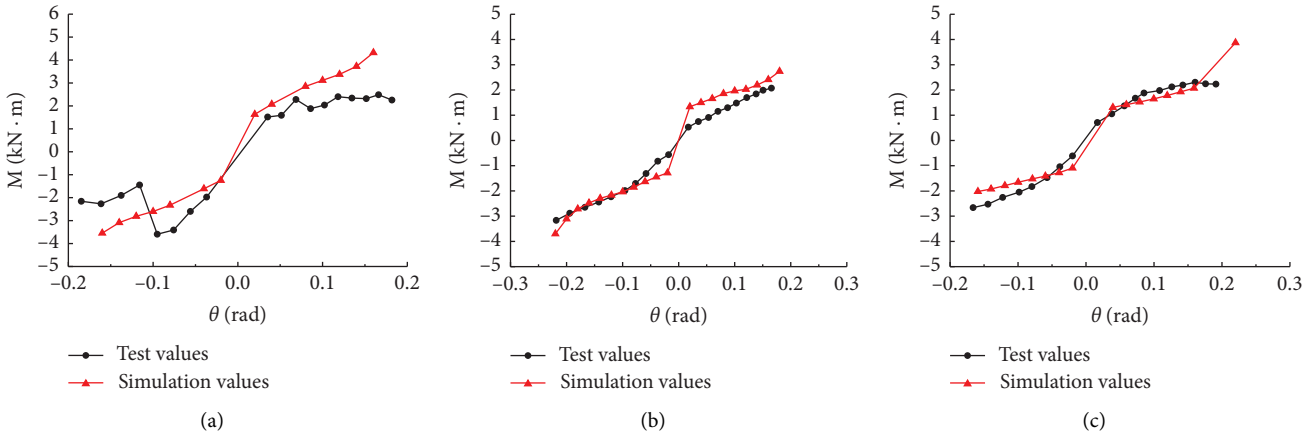

Figure 21: Comparison of the moment-rotation backbone curves of middle joints of steel plate reinforced: (a) Tou mortise-tenon joints. (b) Ban mortise-tenon joints. (c) Dovetail mortise-tenon joints.

Table 10: Comparison of FEM and experimental results.

Mortise-tenon type	Reinforcement method	Total energy of FEM	Total energy of experimental	Total energy ratio (%)	Ultimate load capacity of FEM	Ultimate load capacity of experimental	Ultimate load capacity ratio (%)
Tou mortise-tenon joints	Reinforced	3.75	5.19	72.25	2.59	3.59	72.14
	Unreinforced	5.46	5.5004	99.27	4.32	4.08	105.88
Ban mortise-tenon joints	Reinforced	1.68	2.1958	76.51	0.71	0.6	118.33
	Unreinforced	8.87	4.0293	220.14	3.7	3.16	117.09
Dovetail mortise-tenon joints	Reinforced	1.76	2.37	74.26	0.63	0.44	143.18
	Unreinforced	3.35	5.36	62.50	3.87	2.66	145.49

Note. Total energy ratio and ultimate load capacity ratio are FEM over experimental.

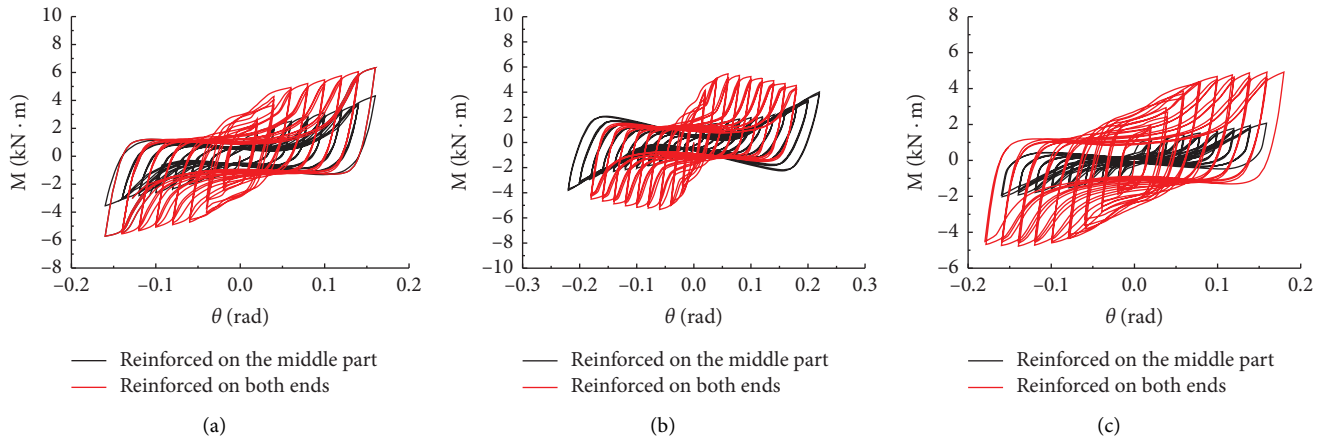

Figure 22: Comparison of h moment-rotation hysteretic loops of joints at different reinforcement positions of steel plates: (a) Tou mortise-tenon joints. (b) Ban mortise-tenon joints. (c) Dovetail mortise-tenon joints.

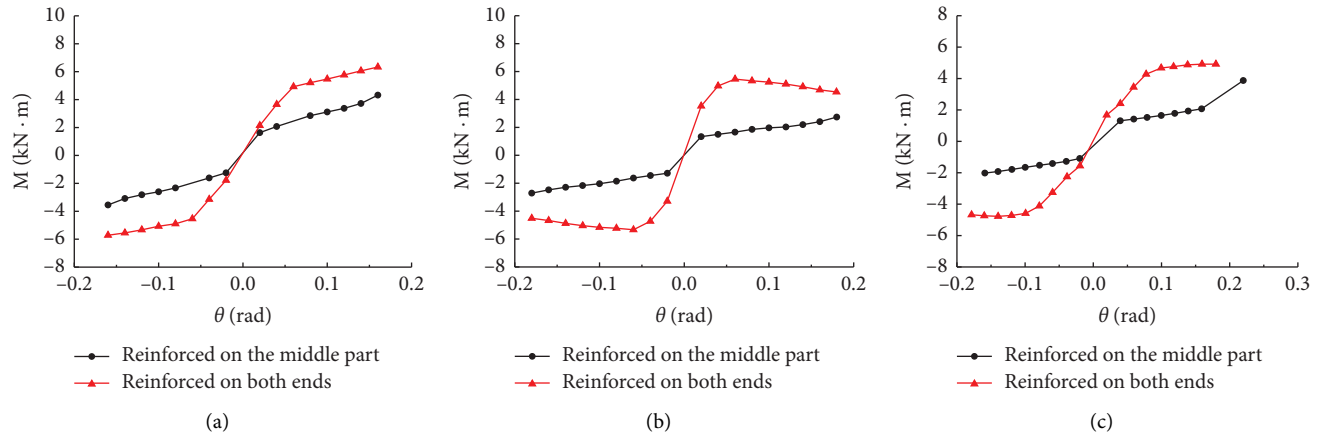

Figure 23: Comparison of moment-rotation backbone curves of joints at different positions of reinforcement by flat steel strips: (a) Tou mortise-tenon joints. (b) Ban mortise-tenon joints. (c) Dovetail mortise-tenon joints.

mortise-tenon joints were reinforced on the upper and lower ends by the flat steel strips. The bearing capacity of Ban mortise-tenon joints skyrocketed after being reinforced on both upper and lower ends by flat steel strips, but the rigidity and bearing capacity of the joints dropped at the later stage of loading. The underlying reason is that the flat steel strips reinforcing Ban mortise-tenon joints on both ends came into operation and underwent torsional bending at the initial stage of loading, so that the initial bearing capacity was higher; with the increase in loading amplitude and pulling-out amount, the wedge pressure friction against the convex tenon inside the concave mortise of Ban mortise-tenon

Table 11: Comparison of results for different reinforcement positions.

Mortise-tenon type	$E_{d,\mathrm{mid}}$	$E_{d,\mathrm{both}}$	$E_{d,\mathrm{both}}/E_{d,\mathrm{mid}}$ (%)	$M_{L,\mathrm{mid}}$	$M_{L,\mathrm{both}}$	$M_{L,\mathrm{both}}/M_{L,\mathrm{mid}}$ (%)
Tou mortise-tenon joints	5.46	11.17	204.58	4.32	6.32	146.30
Ban mortise-tenon joints	8.87	14.67	165.39	3.7	4.91	132.70
Dovetail mortise-tenon joints	3.35	15.07	449.85	3.87	4.92	127.13

Note. $E_{d,\mathrm{mid}}$ is the total energy of reinforced on the middle part, $E_{d,\mathrm{both}}$ is the total energy of reinforced on both end, $M_{L,\mathrm{mid}}$ is ultimate bending moment of reinforced on the middle part, and $M_{L,\mathrm{both}}$ is ultimate bending moment of reinforced on both end.

joints decreased, so that the overall bearing capacity declined. In contrast, the Tou and dovetail mortise-tenon joints maintained certain wedge pressure friction capacity during the loading process for the reason of construction, so the overall hysteresis curve of the model continues going up with the increase in amplitude. On the above, the effect of the flat steel strips reinforcing the mortise-tenon joints on both upper and lower ends is significantly superior to reinforcing the joints on the middle part.

5.3.2. Comparison between Skeleton Curves. Figure 23 compares the skeleton curves for different positions where the mortise-tenon joints were reinforced by the flat steel strips. The results of different reinforcement positions of the three types of mortise-tenon joints are compared as shown in Table 11. Compared with the joints reinforced on the middle part of the beam by the flat steel strips, the bearing capacities of the three distinct types of mortise-tenon joints have promoted to significant degrees in the following order from the smallest to the largest after the flat steel strips reinforced on both upper and lower ends: dovetail mortise-tenon joints, Ban mortise-tenon joints, and Tou mortise-tenon joints. At the turning angle of 0.16 rad, the bearing capacity of dovetail mortise-tenon joints increased by 237% from 2.07 kN·m to 4.92 kN·m, that of Tou mortise-tenon joints increased by 165%, and that of Ban mortise-tenon joints increased by 146%. The three types of mortise-tenon joints entered the yield stage when the turning angle reached 0.06 rad or so. Except for the Ban mortise-tenon joints, the rigidities of the other joints started to decline, while the bearing capacities remained without declining, after the turning angle of loading reached 0.03 rad. This indicates that the joints have excellent deformability.

6. Conclusions

The following conclusions can be drawn through the pseudo-static test and numerical simulation study on unreinforced Tou, Ban, and dovetail mortise-tenon joints and the counterparts reinforced on the middle part by the flat steel strips, and through the numerical simulation for comparative analysis on the differences as the position was varied where the mortise-tenon joints were reinforced by the flat steel strips:

(1) The bearing capacities of the unreinforced mortise-tenon joints were limited. The bearing capacity and deformability of (the unreinforced) Tou mortise-tenon joint were better, with significant rheostriction of the bending moment-turning angle hysteresis curve and severe squeezing between the convex tenon and the concave mortise; its bearing capacity degraded significantly at the later stage of loading; the major destructional forms were fracture and pulling-out of the convex tenon.

(2) Reinforcement on the middle part of the mortise-tenon joints with the flat steel strips has effectively promoted the bearing capacity, rigidity, and energy-dissipating capacity while effectively reducing the pulling-out amount of joints. The reinforcement effect has been most significant on Ban mortise-tenon joints but insignificant on Tou mortise-tenon joints. The destructional forms at the later stage were predominated by the bending-torsion yield failure of flat steel strips.

(3) The effect of the flat steel strips reinforcing the mortise-tenon joints on both upper and lower ends has turned out superior to reinforcing them on the middle part. The hysteresis curves have appeared plumper. The rigidity of joints has raised substantially, and the pulling-out phenomenon has decreased to a large extent, with significantly reduced rheostriction. The ultimate bearing capacities of the joint models reinforced on both ends have increased by 1.5~2.4 times those of the joint models reinforced on the middle part.

Through experiments and FEA, this paper has demonstrated that the hysteretic behaviors of mortise-tenon joints reinforced by flat steel strips have been improved with effectiveness. Therefore, reinforcement with flat steel strips await further investigation. To consummate this finding, further study should focus on the difference between reinforcing side-span joints and reinforcing middle-span joints with flat steel strips. Setting out from the economical efficiency of reinforcement for rural residents, a representative joint reinforcement scheme should be studied out. In addition, further experimental study should be planned to investigate the aseismic performance of the entire wooden structure frame under the reinforcement of flat steel strips.

Data Availability

The data used to support the findings of this study are available from the corresponding author upon request.

Consent

Informed consent was obtained from all individual participants included in the study.

Conflicts of Interest

The authors declare that they have no conflicts of interest.

Authors' Contributions

GSR contributed to the methodology, simulation, results analysis, and original draft of this manuscript. XHX and JYC contributed to the methodology and review of this manuscript. All authors contributed to the scanning and surveying of the temple. All authors read and approved the final manuscript.

Acknowledgments

This study was supported by the National Key Research and Development Program of China (2020YFD1100703-04) and

Yunnan Provincial Education Department Scientific Research Fund Project (2021J0062).

References

[1] Z. W. Guan and E. C. Zhu, "Finite element modelling of anisotropic elasto-plastic timber composite beams with openings," *Engineering Structures*, vol. 31, 2009.

[2] F. Lam, "Modern structural wood products," *Progress in Structural Engineering and Materials*, vol. 3, no. 3, pp. 238–245, 2001.

[3] Z. W. Guan and E. C. Zhu, "Nonlinear finite element modeling of crack behavior in oriented strand board webbed wood i-beams with openings," *Journal of Structural Engineering*, vol. 34, no. 3, p. 8, 2004.

[4] W. Pan, J. Y. Xue, Y. Bai, and T. Zhong, *Seismic Performance and Reinforcement Design Method for Civilian Houses with Wooden structure*, China Science Publishing & Media Ltd, Beijing, China, 2017.

[5] D. F. Gao, H. T. Zhao, and J. Y. Xue, "A seismic characteristics of bucket arch and moruise-tenon joint of ancient Chinese timber buildings: experimental research," *Journal of Natural Disasters*, vol. 17, no. 02, pp. 58–64, 2008, in Chinese.

[6] Q. F. Xie, H. T. Zhao, and J. Y. Xue, "An experimental study on the strengthening of mortise-tenon joints in ancient Chinese wooden buildings," *China Civil Engineering Journal*, vol. 18, no. 1, pp. 28–34, 2008, in Chinese.

[7] H. T. Zhao, J. Y. Xue, and Y. Sui, *Chinese Ancient Structures and Their Seismic experiment, Theory, and Reinforcement Method*, Science Press, Beijing: China, 2012.

[8] E. Poletti, G. Vasconcelos, J. M. Branco, and A. M. Koukouviki, "Performance evaluation of traditional timber joints under cyclic loading and their influence on the seismic response of timber frame structures," *Construction and Building Materials*, vol. 127, pp. 321–334, 2016.

[9] J. A. Wang, J. X. He, N. Yang, and Q. S. Yang, "Study on aseismic characteristics of Tibetan ancient timber structure," *Advances in Materials Science and Engineering*, vol. 2017, Article ID 8186768, 15 pages, 2017.

[10] Q. F. Xie, L. P. Zhang, Z. Miao, W. J. Zhou, and S. Y. Li, "Lateral behavior of traditional Chinese timber-frames strengthened with shape-memory alloy: experiments and analytical model," *Journal of Structural Engineering*, vol. 146, no. 6, Article ID 04020083, 2020.

[11] Q. F. Xie, L. Wang, L. P. Zhang, W. Xiang, and W. B. Hu, "Rotational behaviors of fork-column dou-gong: experimental tests and hysteresis model," *Journal of Performance of Constructed Facilities*, vol. 34, no. 3, Article ID 04020032, 2020.

[12] J. Y. Xue, C. Q. Wu, X. C. Zhang, and Y. T. Zhang, "Effect of pre-tension in superelastic shape memory alloy on cyclic behavior of reinforced mortise-tenon joints," *Construction and Building Materials*, vol. 241, Article ID 118136, 2020.

[13] J. Y. Xue, R. Guo, L. J. Qi, and D. Xu, "Experimental study on the seismic performance of traditional timber mortise-tenon joints with different looseness under low-cyclic reversed loading," *Advances in Structural Engineering*, vol. 22, no. 6, pp. 1312–1328, 2019.

[14] G. Tampone, "Acquaintance of the ancient timber structures," *Guimarães*, vol. 1, pp. 117–144, 2001.

[15] K. E. Larsen and N. Marstein, *Conservation of Historic Timber Structures: An Ecological approach*, Reed Educational and Professional Publishing, London, UK, 2000.

[16] X. W. Li, J. H. Zhao, G. W. Ma, and W. Chen, "Experimental study on the seismic performance of a double-span traditional timber frame," *Engineering Structures*, vol. 98, pp. 141–150, 2015.

[17] Q. Chun, Z. Yue, and J. W. Pan, "Experimental study on seismic characteristics of typical mortise-tenon joints of Chinese southern traditional timber frame buildings," *Science China Technological Sciences*, vol. 54, no. 9, pp. 2404–2411, 2011.

[18] X. C. Zhang, J. Y. Xue, H. T. Zhao, and Y. Sui, "Experimental study on Chinese ancient timber-frame building by shaking table test," *Structural Engineering & Mechanics*, vol. 40, no. 4, pp. 453–469, 2011.

[19] J. Y. Xue, D. Xu, and W. Q. Dai, "Experimental study and numerical simulation analysis on seismic performance of continuous tenon joint in column-and-tie timber structure," *China Civil Engineering Journal*, vol. 52, no. 11, pp. 56–65, 2019, in Chinese.

[20] A. Shi, Z. G. Wang, T. T. Wang, and J. H. Shao, "Reserch on flexural behavior of tenon joint with penetrating pin for residential buildings in Southwest China," *Building Structure*, vol. 18, no. 51, pp. 112–117, 2021, in Chinese.

[21] Y. Lin, Q. Chun, C. W. Zhang, Y. D. Han, and H. Fu, "Research on seismic performance of traditional Chinese hall-style timber buildings in the Song and Yuan dynasties (960–1368 AD): a case study of the main hall of Baoguo Temple," *Journal of Wood Science*, vol. 68, no. 1, p. 1, 2022.

[22] C. C. Chen and H. X. Qiu, "Flexural behavior of penetrated mortise-tenon joints," *Journal of Southeast University (Natural Science Edition)*, vol. 46, no. 02, pp. 326–334, 2016, in Chinese.

[23] C. C. Chen and H. X. Qiu, "Study on flexural behavior of straight mortise-tenon joints," *Journal of Building Structures*, vol. 37, no. S1, pp. 292–298, 2016, in Chinese.

[24] S. Okamoto, M. Nakatani, N. Akiyama, K. Tanaka, and T. Mori, "Verification of the shear performance of mortise and tenon joints with top and bottom notches at the beam end," *Journal of Wood Science*, vol. 67, no. 1, p. 47, 2021.

[25] Q. F. Xie, P. L. Li, and Z. Ya, "Finite element analysis on the cyclic behavior of straight mortise-tenon joints with pullout tenons," *Engineering Mechanics*, vol. 36, no. S1, pp. 138–143, 2019, in Chinese.

[26] B. Hu, J. Cai, and C. Yang, "Theoretical model of bending moment for straight mortise-and-tenon joints with wooden pegs involving a gap," *Materials*, vol. 15, no. 5, p. 1835, 2022.

[27] J. Chen, Y. F. Chen, X. W. Shi, Y. X. Zhao, and T. X. Li, "Hysteresis behavior of traditional timber structures by full-scale tests," *Advances in Structural Engineering*, vol. 21, no. 2, pp. 287–299, 2018.

[28] Z. W. Guan, A. Kitamori, and K. Komatsu, "Experimental study and finite element modelling of Japanese "Nuki" joints part two: racking resistance subjected to different wedge configurations," *Engineering Structures*, vol. 30, no. 7, pp. 2041–2049, 2008.

[29] Y. C. Jin, H. X. Su, and W. Pan, "Experimental research on seismic performance and reinforcement comparison of mortise-tenon joints in timber structures," *Journal of Civil and Environmental Engineering*, vol. 44, no. 02, pp. 138–147, 2022.

[30] Q. F. Xie, B. Z. Zhang, L. P. Zhang, T. T. Guo, and Y. J. Wu, "Normal contact performance of mortise and tenon joint: theoretical analysis and numerical simulation," *Journal of Wood Science*, vol. 67, no. 1, p. 31, 2021.

[31] W. Hu and N. Liu, "Comparisons of finite element models used to predict bending strength of mortise-and-tenon joints," *Bioresources*, vol. 15, no. 3, pp. 5801–5811, 2020.
[32] M. Khelifa and A. Celzard, "Numerical analysis of flexural strengthening of timber beams reinforced with CFRP strips," *Composite Structures*, vol. 111, pp. 393–400, 2014.
[33] A. Aloisio, M. M. Rosso, A. Iqbal, and M. Fragiacomo, "Hysteresis modeling of timber-based structural systems using a combined data and model-driven approach," *Computers & Structures*, vol. 269, Article ID 106830, 2022.
[34] China Technical Committee For Standardization Of Timber, *Physical and Mechanical Tests of wood*, Forestrypedia, Barkhan, Pakistan, 2009.
[35] China Academy Of Building Research, *Specification of Testing Methods for Earthquake Resistant building,* China Academy Of Building Research, Beijing, China, 2015.
[36] Y. L. Gao, L. Y. Ye, and Z. Tao, "Experimental Study and Theoretical Analysis of Traditional Timber Typical Mortise-Tenon Joints Based on the wood Friction Mechanism and Embedded Pressure characteristics," *Kunming university of science and technology*, vol. 18, no. 7, 2017.
[37] K. Hibbitt, *Abaqus Theory manual*, Sorensen Inc, Syracuse, Utah, 2006.
[38] T. P. Nowak, J. Jasieńko, and D. Czepiżak, "Experimental tests and numerical analysis of historic bent timber elements reinforced with CFRP strips," *Construction and Building Materials*, vol. 40, pp. 197–206, 2013.